의학박사 학위논문

Off-target Binding of Glu-Ureido-Lys-Targeted Radioligands to PSMA-like Alternative Proteins: A Potential Therapeutic Target in PSMA-negative and Neuroendocrine Prostate Carcinoma

Glu-Ureido-Lys-유도체 방사성 리간드의 PSMA-유사단백질에 대한 비표적 결합: PSMA-음성, 신경내분비전립선암에 대한 치료표적 가능성

2021 년 08 월

서울대학교 대학원

의학과 핵의학 전공

마틴 (모하마드레자) 바흐트

Off-target Binding of Glu-Ureido-Lys-Targeted Radioligands to PSMA-like Alternative Proteins: A Potential Therapeutic Target in PSMA-negative and Neuroendocrine Prostate Carcinoma

Glu-Ureido-Lys-유도체 방사성 리간드의 PSMA-유사단백질에 대한 비표적 결합: PSMA-음성, 신경내분비전립선암에 대한 치료표적 가능성

August 2021

Graduate School of Medicine

Seoul National University

Nuclear Medicine Major

Martin (Mohamadreza) Khosravi Bakht

Off-target Binding of Glu-Ureido-Lys-Targeted Radioligands to PSMA-like Alternative Proteins: A Potential Therapeutic Target in PSMA-negative and Neuroendocrine Prostate Carcinoma

By

Martin (Mohamadreza) Khosravi Bakht
Academic Adviser: Keon Wook Kang, M.D., Ph.D.
Co-adviser: Gi Jeong Cheon, M.D., Ph.D.

A thesis submitted in partial fulfillment of the requirement for the Degree of Doctor of Philosophy in Medicine,
Graduate School of Medicine
Seoul National University
Nuclear Medicine Major

April 2021

Confirming the Ph.D. Dissertation written by
Martin (Mohamadreza) Khosravi Bakht
August 2021

Chair	Yang Sook Chun
Vice Chair	Keon Wook Kang
Examiner	Gi Jeong Cheon
Examiner	Ho Young Lee
Examiner	Joo Hyun O

Abstract

Prostate-specific membrane antigen (PSMA), a transmembrane protein, is a promising target for imaging and therapy of prostate cancer. PSMA is highly overexpressed in most prostate cancers and is clinically visualized using PSMA-positron emission tomography (PET) probes. Development of small molecules for targeting PSMA is important for PSMA-PET and Glutamate-Ureido-Lysine (GUL)-derivative radioligands are currently leading probes for PSMA-PET.

PSMA is effectively absent from certain high-mortality, treatment-resistant subsets of prostate cancers, such as neuroendocrine prostate cancer (NEPC); however, GUL-based probes still sometimes identify NEPC metastatic tumours. These probes may bind unknown proteins associated with PSMA-suppressed cancers. In this Ph.D. dissertation, the upregulation of PSMA-like aminopeptidase NAALADaseL and the metabotropic glutamate receptors (mGluRs) in advanced prostate cancers including NEPC was identified. This work shows that the expression levels of mGluRs inversely correlate with PSMA expression and are associated with poor survival outcome. Computationally predicting that GUL-based probes bind well to these targets, a fluorescent probe used to investigate these proteins in vitro, where it shows excellent affinity for PSMA, NAALADaseL and specific mGluRs.

This work is available online as:

- Martin K Bakht, So Won Oh, Hyewon Youn, Gi Jeong Cheon, Cheol Kwak, Keon Wook. "Influence of androgen deprivation therapy on the uptake of PSMA-targeted agents: emerging opportunities and challenges." Nuclear medicine and molecular imaging 51, no. 3 (2017): 202-211.
  https://doi.org/10.1007/s13139-016-0439-4

- Martin Bakht, John Hayward, Farsheed Shahbazi-Raz, Daniel Meister, Adam Pillon, Mathew Stover, Adam Tronchin, Lavleen Mader, Bre-Anne Fifield, Sheng-Yu Ku, Gi Jeong Cheon, Keon Wook Kang, Yuzhuo Wang, Xuesen Dong, Himisha Beltran, Lisa Porter, John F Trant. “Identifying Potential Off-Target Protein Binders of Glutamate-Ureido-Lysine, a Prostate Cancer Specific Imaging Agent”. ChemRxiv. Preprint. (2020)
  https://doi.org/10.26434/chemrxiv.13064186.v3

Keyword : Prostate, Cancer, Prostate-specific membrane antigen, Glutamate-Ureido-Lysine, positron emission tomography, metabotropic glutamate receptors
Student Number : 2014-31464

CONTENTS

LIST OF TABLES

LIST OF FIGURES

LIST OF ABBREVIATIONS

AdPC, adenocarcinoma prostate cancer

ADT, androgen-deprivation therapy

AR, Androgen receptor

CRPC, Castration resistant prostate cancer

FBS, Fetal bovine serum

FDG, fluorodeoxyglucose

F-GUL, ^{18}F-PSMA-1007

FOLH1, Folate Hydrolase 1

Ga-GUL,^{68}Ga-labeled PSMA-11

GUL, Glutamate-Ureido-Lysine

IHC, Immuno-histochemical staining

NEPC, neuroendocrine prostate cancer

PDX, Patient-derived xenograft

PET, Positron emission tomography

PSMA, Prostate-specific membrane antigen

1. Introduction

1.1. Study Background

Prostate cancer

Prostate cancer is one of the most commonly diagnosed cancers among men in western industrialized nations and is a leading cause of cancer-related deaths [1]. Men with advanced PCa are usually treated with androgen-deprivation therapy (ADT) [2]. Most patients with metastatic disease treated with ADT eventually relapse with castration-resistant prostate cancer (CRPC). CRPC can be managed with the second-generation inhibitors of the androgen receptor (AR), such as enzalutamide, bicalutamide or abiraterone [3]. These medications provide significant survival benefits, but are not curative [4] and ultimately, the patients die of the disease.

Prostate-specific membrane antigen (PSMA)

PSMA, a transmembrane protein, is a promising target for imaging and therapy of prostate cancer [5, 6]. PSMA is overexpressed in more than 85% of primary prostate cancer tumors and metastatic lesions in lymph nodes and bone [7-9]. PSMA PSMA-positron emission tomography (PET) was FDA-approved in December 2020 and it is predictable to emerge as standard imaging for prostate cancer soon [10].

From technical point of view, targeting PSMA either by antibodies or by small molecules is feasible and clinically comparable to other possible targets for prostate cancer imaging and therapy [11-14]. Particularly, a new class of

functional ligands such as Glu-NH-CO-NH-Lys-[68Ga-(HBED-CC)] or ^{68}Ga-PSMA-11 [15-18], PSMA-DKFZ-617 [19-21], ^{18}F-DCFPyL [22] and EuK-Subkff-^{68}Ga-DOTAGA [23] demonstrated their outstanding affinity to PSMA, therefore made possible the imaging of both local prostate cancer tumors and distant metastatic lesions. These PSMA ligands can also be labeled with therapeutic radionuclides such as lutetium-177 [12]. Since PSMA is physiologically expressed in renal tubular cells [24], renal uptake of these therapeutic radioligands is a limiting factor [25].

Next-generation imaging agents based on small molecule moieties, particularly the PSMA-targeting peptidomimetic Glutamate-Ureido-Lysine (GUL), demonstrate superior pharmacokinetics (fast tumor uptake, and rapid blood clearance) over the radiolabeled PSMA antibodies[26]. GUL's molecular mode of action however, is not completely understood[27, 28]. The leading clinical candidates are ^{68}Ga-labeled PSMA-11 (**Ga-GUL**) [29], where the GUL core is conjugated to an acyclic hexadentate gallium ligand; and ^{18}F-PSMA-1007 (**F-GUL**)[30] where GUL is connected to a *pseudo*peptide functionalized with an ^{18}F isotope (**Figure 1**) [31, 32].

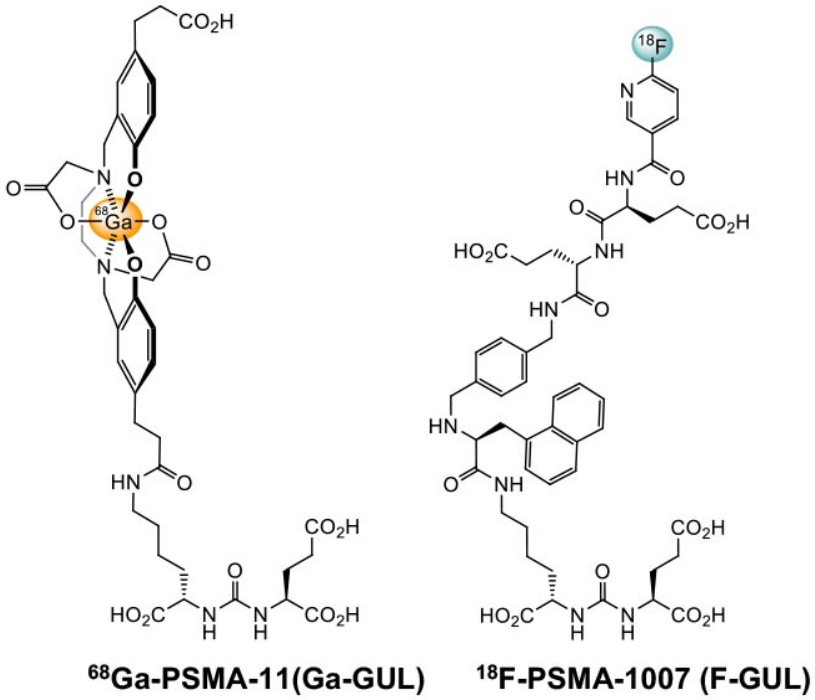

Figure 1 Structure of Ga-GUL (left) and F-GUL (right).

Molecular biology of PSMA expression

Folate hydrolase 1 (*FOLH1*) gene encodes PSMA protein and it is located at the short arm of chromosome 11 in a region that is not normally omitted in prostate cancer (11p11-p12) [33, 34]. It has been well documented that *FOLH1* gene expression is suppressed by androgens [35-37]. By using an enhancer trap approach, Watt *et al.* [38] discovered an enhancer region as a major regulatory element for PSMA expression that considerably activates the *FOLH1* core promoter region. Additionally, they reported that similar to the repression of the FOLH1 gene, PSMA enhanced expression is also inhibited in the existence of androgens. Subsequently, Noss *et al.* [39] sequenced and analyzed the capability of *FOLH1* promoter region to promote the transcription of PSMA mRNA. They reported that in their established prostate cancer model cell line, the *FOLH1* promoter region shaped a 21% downregulation in response to androgens. However, activation of the enhancer region caused a 45% downregulation in response to androgens. Furthermore, by using chromatin immunoprecipitation together with massively parallel sequencing, Yu *et al.* [40] recorded four peaks of AR binding in introns of *FOLH1* gene [41].

Very recent evidence substantiates the claim that we can take advantage of upregulation of PSMA expression for enhancing the efficiency of PSMA-based approaches of endoradio-/chemotherapy. However, the molecular biology of this phenomenon is unclear and the underlying molecular mechanism needs more studies. Figure 2 illustrates PSMA targeted

endoradio-/chemotherapy using a multifunctional theranostic agent with and without pre-targeting enzalutamide, bicalutamide and abiraterone. It seems that the complex including androgen and AR turns off the PSMA enhancer region of *FOLH1* gene (Figure 2a). On the other hand, antiandrogens such as enzalutamide, abiraterone and bicalutamide competitively inhibits androgen binding to AR and the PSMA enhancer region of *FOLH1* gene is switched on (Figure 2b). It can be inferred that common PSMA targeted therapy without pre-targeting by antiandrogens could be less effective than PSMA targeted therapy with prior pre-targeting by antiandrogens since increasing the level of PSMA leads to an increasing endoradio-/chemotherapeutic payload to prostate cancer cells (Figure 2c, d). The multifunctional platform illustrated on Figure 2 contains an imaging probe such as ^{68}Ga [6], a therapeutic radioisotope such as ^{177}Lu [6] and a chemotherapeutic agent such as MMAE [42]. However, the biological mechanism of sensitizing prostate cancer cells for treatment with a single function PSMA-targeted therapeutic agent containing either radioisotope or chemotherapeutic could be similar [43].

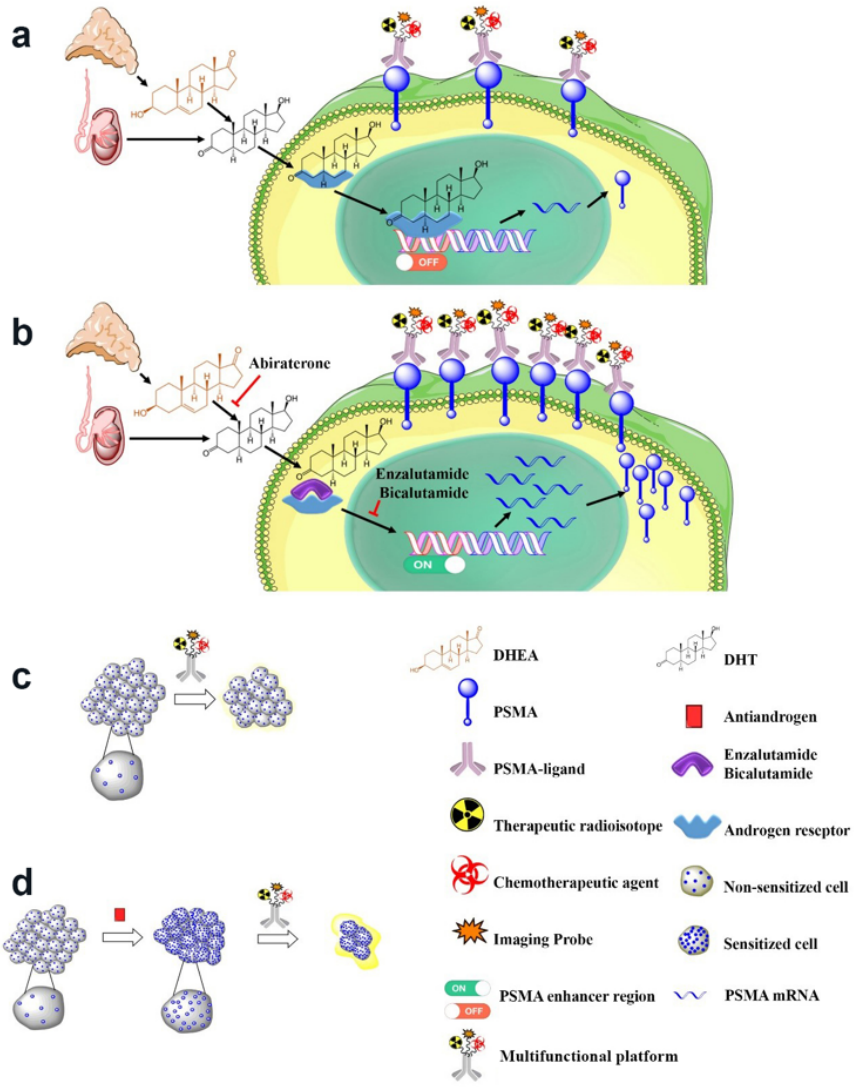

Figure 2 The schematic of a multifunctional PSMA targeted endoradio-/chemotherapy with and without per-targeting antiandrogen.
(a) The androgen binds to AR and this complex inactivates PSMA enhancer region of *FOLH1* gene; (b) Enzalutamide competitively inhibits androgen binding to AR and PSMA enhancer region of *FOLH1* gene is activated; (c) Common PSMA targeted therapy; (d) PSMA targeted therapy with prior pre-targeting by antiandrogens [43].

PSMA modulates glutamate signaling induced by the metabotropic glutamate receptor (mGluR) pathway,[44] cleaving glutamate from both dietary folic acid and the neurotransmitter *N*-acetyl-L-aspartyl-L-glutamate (NAAG). PSMA overexpression is a hallmark of prostate cancer including metastatic castration resistant prostate adenocarcinoma.[45, 46] Despite this, both immunohistochemical and genomic data have demonstrated that PSMA is expressed at only very low levels, if at all, in neuroendocrine prostate cancer (NEPC) [47], an aggressive form of androgen-receptor (AR)-independent prostate cancer with exceedingly high mortality rates[47, 48]. In our previous study, we evaluated suppression of PSMA in NEPC [49].

While *de novo* NEPC is rare, this hard-to-treat phenotype can emerge as a prostate cancer resistance mechanism to AR-targeted therapies, shedding the PSMA biomarker concurrent with a downregulation of the AR.[48, 50, 51] PSMA expression can be heterogeneous and PSMA imaging can be seen in patients with heterogeneous expression [52]. However, as GUL-PET modalities target PSMA, they are not expected to be effective for diagnosing NEPC due to PSMA-negativity. A less specific agent, ^{18}F-fluorodeoxyglucose, which exploits cancer cells' increased glucose-uptake, is often used for NEPC imaging similar to small cell lung cancer[53, 54]. In our previous study, we reported differential expression of glucose transporters and hexokinases in prostate cancer with a neuroendocrine gene signature and it was a mechanistic perspective for FDG imaging of PSMA-suppressed tumors [55].

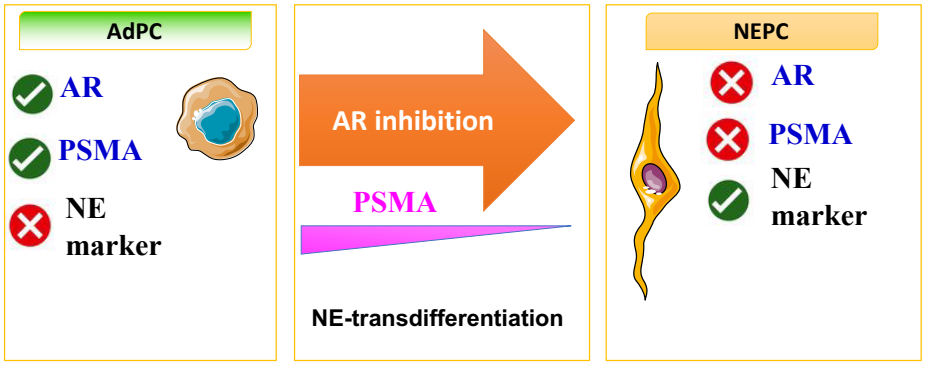

Figure 3 A schematic of NE-transdifferentiation impact on PSMA expression.

Unexpectedly, a recent study demonstrated that GUL-based imaging can delineate IHC validated PSMA-negative metastatic tumors despite the tumour's PSMA-negativity[56]. Similarly, another recent study showed neuroendocrine marker profiles do not essentially predict outcome of PSMA-targeted radioligand therapy [57]. Although PSMA expression is correlated with GUL-radioligand uptake[58], the correlation is not perfect and tumours with low PSMA expression may also be detected using GUL-based probes[57]. GUL-based probes have also resulted in false positive interpretations among patients with a history of radiotherapy[59]. Together, the evidence suggests that GUL interacts fortuitously with other prostate cancer-associated proteins. Identifying these targets, and determining whether they are indicative of NEPC, is a pressing clinical goal.

Role of preclinical imaging in development and reassessment of radioligands

Molecular imaging is a growing multidisciplinary field which includes molecular biology, biochemistry, computer science, bioinformatics, engineering, and biomedicine.

Figure **4**A summarized a variety of currently being used molecular imaging modalities. No single modality can achieve multiscale or holistic data due since the spatial resolution goes up by increasing the depth of penetration (**Figure 4A**). However, the combination or multimodal correlation of multiple modalities can overcome this problem. Therefore, we can only utilize some of these modalities in preclinical settings for a variety of proposes such as drug

development, pharmacodynamics and quantification of biologic processes [60]. For experimental design of radioligands, application of molecular imaging is a well-stablish approach to achieve an optimal PET radioligand (**Figure 4B**).

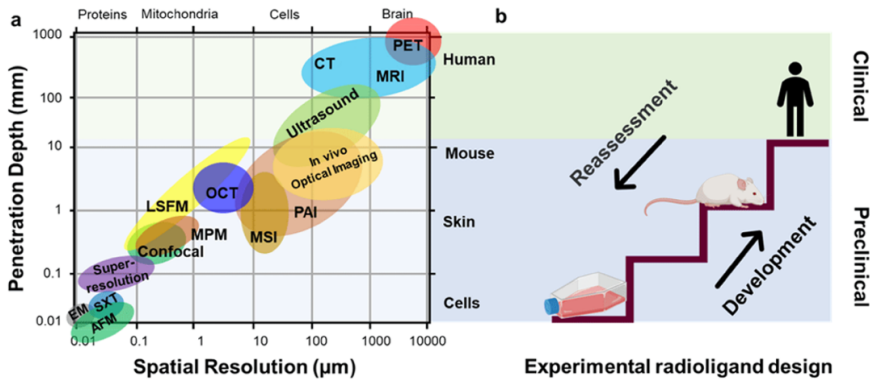

Figure 4 The role of preclinical imaging in the development and reassessment of radioligands.
(a) A summary of clinical and preclinical imaging modalities shows penetration depth directly correlates with spatial resolution (Adopted from Walter et al. 2020 [60]. SXT; Soft X-ray Tomography; EM, Electron Microscopy; CT, Computed Tomography; OI, Optical Imaging such as bioluminescence and fluorescence imaging; LSFM, Light Sheet Fluorescence Microscopy; MPM, MultiPhoton Microscopy, Confocal, Confocal Microscopy; MRI, Magnetic Resonance Imaging; PAI, Photoacoustic Imaging; OCT, Optical Coherence Tomography; AFM, Atomic Force Microscopy; MSI, Mass Spec Imaging; Super-resolution, Microscopy. (b) A schematic of the required steps for experimental radioligands design. Penetration depth is a limitation for a majority of preclinical imaging modalities, while these techniques can have a significant contribution to the development and assessment of radioligands due to their superior resolution.

1.2. Purpose of Research

The mGluRs and the aminopeptidase NAALADaseL1 are both PSMA-related type II transmembrane peptidases involved in glutamate signaling. We hypothesized that these proteins might be responsible for GUL's off-target positive results in NEPC. In this study, we investigated this question with a cross-disciplinary combination of computational chemistry, synthesis and histochemical application of a new fluorescent probe, mining of clinical data, *in vitro* over-expression of the suspected proteins, and *in vivo* patient-derived xenograft (PDX) models.

2. Materials and Methods

2.1. Biological materials and methods

Cell culture

The LNCaP and DU-145 cell lines were purchased from ATCC (Manassas, VA, USA). LNCaP cells were grown in RPMI 1640 in the presence of 10% fetal bovine serum (FBS). DU-145 cells were grown in Eagle's minimum essential medium (E-MEM) supplemented with 10% FBS. Progression to NEPC was achieved by culturing LNCaP cells in RPMI1640 medium with 10% charcoal-stripped serum for 4 months. We previously characterized and validated these models[51]. Briefly, LNCaP cell morphology gradually changed into a mixture of a NE-like phenotype and a non-NE-phenotype as a result of chronic hormonal depletion. After 4 months, a subclone with a NE-like phenotype was isolated (LNCaP-NE). LNCaP cells, maintained in RPMI-1640 + fetal bovine serum, were used as a control and are referred to as LNCaP-AdPC.

Plasmids and transfection

GRM8-Tango was a gift from Dr. Bryan Roth (Addgene plasmid # 66393) [61]. Transfection of plasmids was performed using Lipofectamine 3000 (Life Technologies) according to the manufacturer's instructions.

Knockdown experiments

To knockdown human *NAALADL1,* the small interfering RNA (siRNA)-mediated knockdown was designed by i-Score Designer (Nagoya University Graduate School of Medicine, Japan) [62]. Then the scrambled siRNA

sequences were designed using InvivoGen's siRNA Wizard (InvivoGen, San Diego, CA, USA). The siRNA sequences are listed on f

Table 1 Specific small interfering RNAs *of* NAALADL gene1 The siRNA transfections were performed in 6-well plates when the LNCaP cells reached approximately 70% confluence using Lipofectamine RNAiMax Reagent (Thermo Fisher Scientific) and 30 pmol of each siRNA according to the manufacturer's protocol, and cells were harvested 48 h later.f

Table 1 Specific small interfering RNAs of *NAALADL* gene

siRNA	**Sense**	**Antisense**	**Position**
si-*NAALADL1*#1	CAGAAGAGUUCUUCAACAA	UUGUUGAAGAACUCUUCUG	1312
Scrambled siRNA#1	GAACAGCTAACGAATTCTA	GTTCGTTTAGTCGGCAATTTA	Not applicable
si-*NAALADL1*#2	GCUUCUUCCUGCCCCUCAA	UUGAGGGGCAGGAAGAAGC	1777
Scrambled siRNA#2	GCTTCACCCCCTAGTCTCT	GGAAGGGTTCGACAGAGAGGT	Not applicable

Quantitative real-time PCR analysis

RNA was isolated using Qiagen RNeasy Plus Mini Kit as per manufacturer's instructions. cDNA was synthesized using Superscript II (Invitrogen) as per manufacturer's instructions. SYBR Green detection (Applied Biosystems) was used for real-time PCR and was performed and analyzed using Viia7 Real Time PCR System (Life Technologies) and software. The primers used are listed on **Error! Reference source not found.**.

Table 2 Primer sequences for Quantitative real-time PCR

Gene name	Forward 5 → 3	Reverse 5 → 3
NAALADL1	TGGAGCCTGATCGCTACGTG	ATTGATCTGCGAGGACGCCA
FOLH1	GGAGAGGAAGTCTCAAAGTGCC	TGGTTCCACTGCTCCTCTGAGA
GAPDH	GGAGTCAACGGATTTGGT	GTGATGGGATTTCCATTGAT

Immunoblotting and immunocytochemistry

Anti-Flag (F1804), secondary rabbit and mouse antibodies were purchased from Sigma-Aldrich. Anti-PSMA (D4S1F) was purchased from Cell Signaling (12702). Immunoblotting and immunocytochemistry techniques were described previously[51]. In brief: cells were lysed in TNE buffer (50 mM Tris, 150 mM NaCl, 5 mM EDTA) with protease inhibitors (leupeptin 2 μg/mL, aprotinin 5 μg/mL, PMSF 100 μg/mL). Protein concentrations were assessed using the Bradford assay and equal amounts of protein were analyzed using SDS-PAGE and transferred to PVDF membranes. Membranes were blocked for 1 h at room temperature in 1% BSA and incubated in primary antibody overnight at 4 °C, followed by secondary at a concentration of 1:10,000 for 1 h at room temperature. Visualization was conducted using chemiluminescent peroxidase substrate (Pierce) as per manufacturer's instructions. Images were captured on Alpha Innotech HD 2 using AlphaEase FC software.

Primary antibodies for immunohistochemistry were diluted in 3% BSA-0.1% Tween-20 in 1x PBS and used at a concentration of 1:200. Secondary antibodies were used at a concentration of 1:750. Slides were imaged using the LEICA DMI6000 inverted microscope with LAS 3.6 software.

Cy3-GUL cytotoxicity evaluation

Cell viability was measured by MTT assay of Sigma-Aldrich (St. Louis, MO, USA) according to the manufacturer's protocol. Briefly, LNCaP and DU145

were seeded into 96-well plates at a density of 4,000 cells/well and cultured overnight for adhesion. Different concentrations of Cy3-GUL ranging from 0.1 nM to 10 μM were incubated with cells for 24 h at 37 °C. Cells without FBS treatment were used as controls. Following incubation, MTT solution (20 μl of 5 mg/ml in PBS) was added to each well and incubated for 4 hr. Extraction buffer (100 μl) was added for 2 h to dissolve the formazan crystals, and the absorbance at 590 nm was assessed using Victor plate reader (PerkinElmer).

Cytometric analysis

For verification of Cy3-GUL affinity to PSMA, cytometric analysis was performed using a BD LSRFortessa™ X-20 Flow Cytometer System. A 1.5×10^5 LNCaP and DU145 cells were incubated with 100 nM Cy3-GUL for 1 h at 37 °C. Cells were rinsed with 200 μL PBS and analyzed by flow cytometry. The data analysis was performed using a BD LSRFortessa™ Cell Analyzer System and FlowJo® software.

Cy3-GUL *in vitro* imaging

50,000 LNCaP cells were seeded in 12 well glass-bottom dishes (Corning) overnight at 37 °C. Cells were washed 2 times with PBS and incubated for 1 h at 37 °C. Cells were treated with 100 nM Cy3-GUL and 100 ng/mL Hoechst 33342 (Thermo Scientific) for 5, 10 and 30, 60, 120 min, respectively. Cells were washed twice with PBS and prepared for live imaging by adding 1 mL of PBS. Fluorescence images were obtained on a LeicaDM IL microscope

(Wetzlar, Germany). Cy3 signal was quantified using ImageJ and the mean fluorescent signal measurement from 30–40 cells.

2.2. Data mining analysis

To estimate PSMA-like proteins, we performed sequential homology using the Basic Local Alignment Search Tool (BLAST) and FASTA sequence of PSMA (2XEI)[63] (Figure 5A). We considered proteins with a BLAST total score of 200 as PSMA homologous and five proteins recognized as PSMA-like proteins, including *NAALADL1*, *NAALADL2, NAALAD2, FOLH1B,* and *TFRC*. In addition, for estimation of structural homology with PSMA, we used BioZernike [64]. BioZernike is a search system that enables real-time retrieval of similar protein assemblies to a target assembly. The system uses coarse grained volumes created out of atomic models, though the method presented here is applicable to any kind of volume, be it experimental or simulated. Proteins with a Geometric score greater than 80% are considered PSMA-like. *NAALADL1, NAALAD2*, and TFRC were recognized as PSMA-like proteins using BioZernike [64]. Figure 5B illustrates the expression of the identified PSMA-like proteins in the LTL331 model. The fold change is computed as the ratio of the changes between LTL331R (NEPC model) and the LTL331 (AdPC) over the LTL331 expression. We considered genes with a fold change over two as a differentially expressed gene in NEPC. Therefore, *NAALADL1* was identified as a PSMA-like protein among differentially expressed genes in NEPC. Since glutamate is part of GUL-targeted

radioligand, we also investigated mGluR proteins' interactions. However, mGluR proteins have no structural or sequential homology with PSMA.

We mined our published datasets [65-68] to assess transcript abundance for PSMA gene (*FOLH1*), NAALADase-like1 (*NAALADL1*), 8 members of the metabotropic glutamate receptors (mGluRs) (genes: *GRM1 to 8*), the NE marker synaptophysin gene (*SYP*), *SRRM4* as a positive marker of treatment-induced NEPC and *REST* as negative marker of NEPC across stages of prostate cancer progression (31 benign, 66 localized AdPC, 74 CRPC, 35 NEPC and in other cancer types). Reads were mapped to the human genome reference sequence (hg19/GRC37) using STAR v2.3.0e. For each sample, HTSeq and Cufflinks were utilized to produce read counts and FPKM values, respectively.

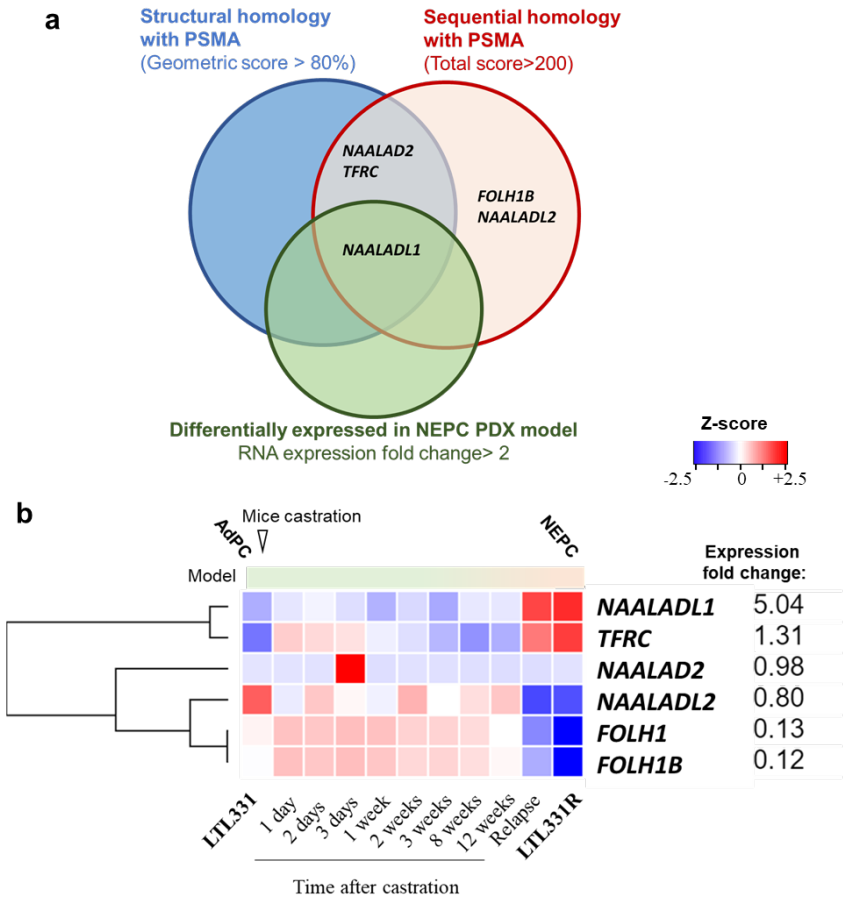

Figure 5 *NAALADL1* identified as a PSMA-like protein among differentially expressed genes in NEPC.
(a) The Venn diagram shows the overlap between the identified PSMA homologous by sequential [63] and structural [64] approaches. In addition, it shows their overlap with differentially expressed genes in NEPC. (b) A heatmap of the expression of the identified PSMA-like proteins in LTL331 model. The fold change between LTL331R (NEPC model) and the LTL331 (AdPC) are listed on the left.

The survival data and pairwise-correlations of gene expression

The specialized web interface, Cambridge Carcinoma of the Prostate App (camcAPP, http://bioinformatics.cruk.cam.ac.uk/apps/camcAPP/) as a source for multiple AdPC genomic datasets was used in this study. The camcAPP was used for recursive partitioning-based survival analysis and Kaplan-Meier plots, pairwise-correlations of gene expression and heatmaps of gene expression data. Survival data and heatmaps were generated using camcAPP, which is implemented in R code as a Shiny application [69]. Kaplan-Meier biochemical relapse-free survival plots were generated using a recursive partitioning (RP) analysis named unbiased recursive partitioning [70]. This conditional inference framework was used to determine if the samples could be split into groups based on the expression data from each of the genes of interest. The algorithm tailored for our case can be described as follows: a statistical test of independence was run between gene expression levels and the survival times. When the p-value of initial test of independence (ITI) was found to be less than 0.05, an optimal cutoff point was determined in the expression data such that a weighted log-rank statistic (a loss function based on log-rank) comparing the two groups resulting from dividing the sample of patients by the cutoff point would be maximized. Afterwards, the samples were split at the optimal cutoff point on the expression scale and represented as a log-rank comparing those two groups. When the algorithm did not

confirm dependence between survival times and gene expression, we split samples into two groups based on median expression level of the gene. In the cases with ITI p-values more than 0.05 we are unable to state a definitive relationship between the expression of the gene and survival. The value quoted on the Kaplan-Meier plots of this manuscript indicate where the recursive partitioning algorithm has found two distinct groups of samples as high and low expression levels and the log-rank test was employed to identify statistical difference between the high and low expressing groups. Pearson correlation was used for pairwise-correlations of the studied gene expression analysis.

2.3. Animals and PDX models

Fresh AdPC or NEPC tissues from patients were grafted under the kidney capsules of non-obese diabetic/severe combined immunodeficient (NOD/SCID) mice. This study followed the ethical guidelines stated in the Declaration of Helsinki. Specimens were obtained from patients with their informed written consent following the protocol (#H09-01628) approved by the Institutional Review Board of the University of British Columbia (UBC). Animal studies were completed under protocol # A17-0165 as approved by UBC Animal Care and Use Committee.

The expression of the PSMA gene in 5 AdPC PDX models (LTL-313-B, LTL-313-B-R, LTL-418, LTL-418-R and LTL-331-7) and 2 NEPC PDX models (LTL-331-7-R and LTL-352) was studied by real time PCR analysis. Transcription of *FOLH1* and *SSTR2* genes in 18 PDX models including 3 NEPC models were analyzed. Transcriptomic analysis for all PDX models,

with the exception of the LTL331-331R castration time-series samples, was achieved by GE 8×60K microarray and transcriptomic analysis of the LTL331-331R time-series performed using RNA-sequencing data [71, 72]. We previously characterized and validated these models as having AdPC and NEPC mRNA and protein signatures [73-75].

2.4. Synthesis of a novel Cy3-GUL probe

General Experimental

Solvents were purchased from Caledon Labs (Caledon, Ontario), Sigma-Aldrich (Oakville, Ontario) or VWR Canada (Mississauga, Ontario). Other chemicals were purchased from Sigma-Aldrich (Oakville, Ontario), AK Scientific (California, USA), Oakwood Chemicals (South Carolina, USA), Alfa Aesar (Massachusetts, USA) or Acros Chemicals (New Jersey, USA) and were used without further purification unless otherwise noted. Anhydrous toluene, tetrahydrofuran (THF), diethyl ether and N,N-dimethylformamide (DMF) were obtained from an Innovative Technology (Newburyport, USA) solvent purification system based on aluminium oxide columns. CH_2Cl_2, pyridine, acetonitrile, N,N-diisopropylethylamine (DIPEA) and NEt_3 were freshly distilled from CaH_2 prior to use. Purified water was obtained from a Millipore (Massachusetts, USA) deionization system. DMSO was used after sitting over previously washed, freshly activated, 4 Å molecular sieves. All heated reactions were conducted using oil baths on IKA RET Basic (North Carolina, USA) or equivalent stir plates equipped with a P1000 temperature probe. Thin layer chromatography was performed using EMD aluminum-

backed silica 60 F254-coated plates and were visualized using either UV-light (254 nm), $KMnO_4$, vanillin, Hanessian's stain, or Dragendorff's stain. Preparative TLC was done using glass-backed silica plates (Silicycle (Quebec, Canada)) of either 250, 500, 1000 or 2000 μm thickness depending on application. Column chromatography was carried out using standard flash technique with silica (Siliaflash-P60, 230-400 mesh Silicycle (Quebec, Canada)) under compressed air pressure. Standard work-up procedure for all reactions undergoing an aqueous wash involved back extraction of every aqueous phase, a drying of the combined organic phases with anhydrous magnesium sulphate, filtration either using vacuum and a sintered-glass frit or through a glass-wool plug using gravity, and concentration under reduced pressure on a rotary evaporator (Buchi (Flawil, Switzerland) or Synthware (New Jersey, USA)). ^{1}H NMR spectra were obtained at 300 MHz or 500 MHz, and ^{13}C NMR spectra were obtained at 75 or 125 MHz on Bruker instruments. NMR chemical shifts (δ) are reported in ppm and are calibrated against residual solvent signals of $CHCl_3$ (δ 7.26), DMSO-d_6 (δ 2.54), acetone-d_5 (δ 2.05), or methanol-d_3 (δ 3.31). HRMS were conducted on a Waters XEVO G2-XS TOF instrument with an ASAP probe in CI mode.

Specific Protocols

For the synthesis of the dye intermediates in Figure 6, please see our previous publication [51].

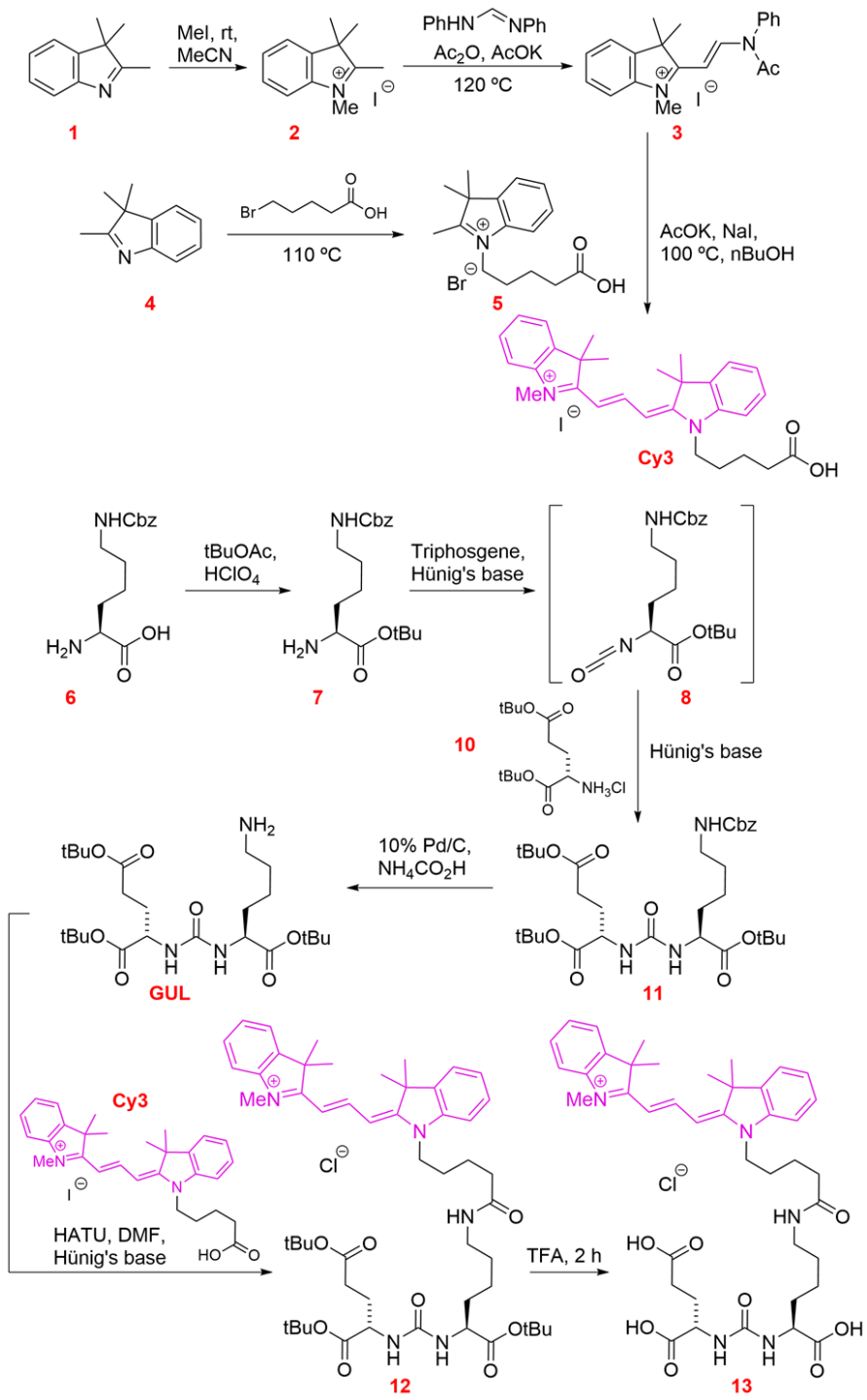

Figure 6 The chemical synthesis of Cy3-GUL.

Protected Cy3-GUL (12)

To a solution of the **Cy3** iodide salt (35 mg, 0.06 mmol) in DMF (1.0 mL) at 0 °C was added HATU (26 mg, 0.066 mmol, 1.1 equiv.) and Hünig's base (24 μL, 0.13 mmol, 2.2 equiv.), followed by the addition of the **GUL** amine (30 mg, 0.06 mmol), synthesized according to the protocol of Maresca.[76] The resulting mixture was allowed to warm to room temperature and stirred for 18 h, after which time the reaction mixture was diluted with H_2O and extracted with EtOAc. The organic layer was washed with saturated brine and dried (Na_2SO_4) and concentrated in vacuo. The resulting material purified using preparative TLC (2% MeOH/DCM). The plate was developed 8 times, until the pure product band (top) was visible. The product was washed from the silica using MeOH and the solvent removed to yield the product as a glassy pink film (7 mg, 11%). N.b. The desired product could be observed in other bands on the TLC plate-co-eluting, but in those cases it was contaminated with other unidentified byproducts. Purification improvements remain underway in the group.

Pink glass. R_f (4% MeOH/DCM) = 0.43 ^{1}H NMR (500 MHz, $CDCl_3$) δ_{ppm} = 8.39 (t, J = 13.5, 1H), 7.44 – 7.38 (m, 2H), 7.36 (ddd, J = 7.5, 3.7, 1.2, 2H), 7.29 – 7.22 (m, 2H), 7.15 (d, J = 7.9, 2H), 6.60 (d, J = 13.5, 1H), 6.50 (d, J = 13.5, 1H), 6.48 – 6.46 (br m, 1H), 5.47 (br d, J = 7.9, 1H), 5.36 (br d, J = 8.2, 1H), 4.31 (td, J = 8.3, 5.1, 1H), 4.24 (td, J = 8.0, 4.4, 1H), 4.08 – 4.01 (m, 2H), 3.68 (s, 3H), 3.32 – 3.15 (m, 2H), 2.37 – 2.30 (m, 3H), 2.09 – 2.01 (m, 1H), 1.91 – 1.79 (m, 6H), 1.77 – 1.60 (m, 2H) 1.72 (s, 2×3H), 1.71 (s, 2×3H), 1.61 – 1.46 (m, 2H), 1.46 – 1.34 (m, 2H), 1.44 (s, 9H), 1.414 (s, 9H),

1.406 (s, 9H). ^{13}C NMR (126 MHz, $CDCl_3$) δ_{ppm} = 174.706, 174.000, 173.666, 172.735, 172.670, 172.379, 157.508, 150.854, 142.862, 142.003, 140.596, 140.558, 129.241, 129.077, 125.625, 125.595, 122.178, 122.109, 111.245, 111.059, 104.147, 103.624, 81.615, 81.337, 80.481, 53.770, 53.143, 49.248, 49.122, 44.391, 38.774, 36.280, 31.854, 31.851, 31.505, 28.870, 28.411, 28.307, 28.285, 28.209, 28.148, 28.126, 27.033, 23.427, 22.286. HRMS (ESI+) Calc'd for $C_{53}H_{78}N_5O_8$ [M^+] = 912.5850, Found 912.5853.

Cy3-GUL

The tri-ester (6 mg) was treated with distilled TFA (1 mL) at room temperature and stirred for 18 h. The TFA was removed under reduced pressure and the residue was used as is.

Pink glass. R_f (4% MeOH/DCM) = 0.31; ^{1}H NMR (500 MHz, CD_3OD) δ_{ppm} = 8.55 (t, *J* = 13.4, 1H), 7.54 (dd, *J* = 7.4, 1.0, 2H), 7.45 (tdd, *J* = 7.8, 3.5, 1.2, 2H), 7.36 (d, *J* = 7.9, 2H), 7.31 (tdd, *J* = 7.6, 4.0, 1.0, 2H), 6.44 (dd, *J* = 13.4, 2.8, 2H), 4.34 – 4.28 (m, 1H), 4.23 (dd, *J* = 8.5, 4.8, 1H), 4.17 (t, *J* = 7.4, 2H), 3.69 (s, 3H), 3.17 (t, *J* = 6.8, 2H), 2.42 – 2.36 (m, 2H), 2.28 (t, *J* = 6.9, 2H), 2.20 – 2.08 (m, 1H), 1.92 – 1.83 (m, 1H), 1.774 (s, 2×3H) 1.769 (s, 2×3H), 1.65 – 1.58 (m, 2H), 1.53 – 1.34 (m, 8H). ^{13}C NMR (126 MHz, CD_3OD) δ_{ppm} = 179.7, 176.8, 176.4, 176.0, 175.8, 175.4, 160.1, 152.2, 144.1, 143.4, 142.19, 142.11, 130.02, 129.96, 126.80, 126.75, 123.54, 123.38, 112.44, 112.32, 103.8, 103.6, 50.6, 44.9, 40.0, 37.6, 36.4, 33.2, 31.8, 31.1, 30.8, 29.9, 28.9, 28.3, 28.2, 27.9, 25.6, 24.2, 23.9.

. HRMS (ESI+) Calc'd for $C_{41}H_{54}N_5O_8$ [M^+] = 744.3972, Found 744.3966.

2.5. Computational Analyses

Initial structural similarity assessment

TopMatch-web provides used for pairwise structure comparison of PSMA (PDB ID: 2XEG,A) & NAALADase L (PDB ID : 4TWE,A) to generate the 2D and 3D alignment [77].

Docking simulations

Docking simulations (both rigid and induced fit) were performed to study the binding of ligands GUL-Cy3, ^{68}Ga-GUL, and ^{18}F-GUL, to known and potential binders (PSMA, NAALADaseL and mGluRs 1-8). Docking was performed using the Glide[78] module of the Schrödinger suite. Molecular dynamics of the ligands bound to mGluR8 were performed using Amber16 to further study protein-ligand interactions and complex stability.

Protein preparation

The 3D coordinates of the of receptors complexes for PSMA, NAALADaseL and mGluR 1,2,3,5,7,8 (PDB ID: *2XEG*, *4TWE*, *1EWK*, *5CNI*, *3MLK*, *2E4Z*, *6BSZ*, respectively) were retrieved from Protein Data Bank and all crystal waters were removed which had no immediate the interaction between the protein and ligand. Structures of mGluR 4 and 6 were generated through homology modelling as they did not have published crystal structures. The structures were prepared with the Protein Preparation Wizard workflow as follows: adding hydrogen, assigning partial charges using the OPLS3e force

field, assigning protonation states[79]. Minimization of the structure was complete after root mean square deviation (RMSD) of heavy atoms exceeded 0.3 Å [80]. The ligand in the crystal structure was used to determine the location of a docking grid box and was then removed prior to grid generation in next step.

Ligand preparation

The studied ligands are listed in Figure 1. The 3D molecular structures of all compounds were built with the Schrödinger software. Energy minimization was performed using the OPLSe3 force field. Then, all the compounds were prepared using the Ligprep module [81].

Rigid receptor docking studies

Ligand docking was performed using the GLIDE module following grid-based docking protocol. The grid was generated around the predicted active site. Ligands were docked against the predicted active site of the modeled receptor using the Glide XP docking protocol. The scaling factor for protein van der Waals radii was set to 0.8 in the receptor grid generation. The ligand in the active site was used as the centroid to generate the grid files for the following docking process. The default grid size was adopted from the Glide program. No constraints were applied for all the docking studies. For each compound, a maximum of 10 poses were saved after docking process.

Induced-fit docking study

To consider the flexibility of both the ligand and receptor in the docking study, the IFD protocol[82] was adopted. In the IFD protocol, ligands were docked into the rigid protein using Glide with softened potentials with van der Waals radii scaling of 0.8 for the proteins. The top 10 poses of each ligand were then used to sample protein plasticity using Prime in the Schrödinger suite. Residues having at least one atom within 5 Å of any of the 10 ligand poses were subject to a conformational search and energy minimization process and residues outside this zone were fixed allowing for flexibility within the binding pocket. In this redocking stage, Glide docking parameters were set to the default hard-potential function. The Glide XP (extra precision) setting was used for all docking calculations. The binding affinity of each complex was reported as the Glide Score.

Homology modeling

Protein structures are modeled by homology modeling method using Prime in the Schrödinger software suite. Blast search is performed to identify template protein structures [83]. mGluR4 and mGluR6 were modeled using PDB: *6BT5*, human mGlu8 as template sequence. NAALAD1 protein is modeled using PDB: *2EXG* human glutamate carboxypeptidase. Loops are refined and verification is done by protein refinement program of Schrödinger software.

Molecular dynamics protocol

The top pose generated by docking for each probe was utilized. GUL-Cy3 and ^{18}F-GUL were parameterized using Antechamber and charges generated using AM1-BCC model in AMBER[84]. Due to the metal present, ^{68}Ga-GUL was parameterized in AMBER16 using MCPB.py with a previously outlined protocol[85]. The complexes were solvated using a 10 Å isotropic TIP3P water box. Charges were neutralized using Na+ or Cl− atoms. Three minimizations were conducted using decreasing constraints. Each minimization included 10,000 steps conjugate gradient and 10,000 steps steepest descent, with restraints of 100, 3 and 0 kcal/mol−Å^2, respectively on the protein-ligand complex. A distance cut-off of 10 Å was used for all simulations along with a 2 femtosecond timestep and SHAKE constraints. Simulations were conducted at constant pressure using the Berendsen barostat. The system was then heated to 310 K over 50 ps using the Langevin thermostat, followed by 250 ps of density equilibration at 1 bar. Lastly, a production run of 250 ns was run for all complexes. RMSD, clustering and H-bond analysis was performed using cpptraj in AmberTools with sampling every 5 frames. Clustering was performed on the ligand heavy atoms and a 1 Å cut-off was used between clusters.

2.6. Statistical analysis

Statistical analysis was done using GraphPad Prism (CA, USA) and Origin Pro 2020 (OriginLab Corporation, Northampton, USA). The results are expressed as the mean ± standard error of the mean (SEM). The box-whisker plots show the median (horizontal line), the interquartile range (margins of box) and the absolute range (vertical line). Differences between two groups were compared by unpaired Student's t-test. One-way ANOVA followed by a Benjamini-Hochberg or Tukey adjustment. Neurite length was measured by manual tracing and determined using NIH ImageJ software as previously described [47, 86]. Pearson correlation was used for nearest neighbor analysis and pairwise-correlation of the studied genes. Kaplan-Meier plots and heatmaps were generated using camcAPP [69], Broad Institute Morpheus software (MA, USA) and R2: Genomics Analysis and Visualization Platform (http://r2.amc.nl).

3. Results and Discussions

3.1. F-GUL and Ga-GUL are predicted to have high affinity for PSMA.

GUL-based probes interact with three components of PSMA's active site: the zinc ions, the pharmacophore (S1′) pocket, and the hydrophobic S1 accessory pocket.[87] PSMA's active site hosts two Zn^{2+} ions, responsible for substrate cleavage.[88, 89] The S1′ site, highly specific for glutamate, determines substrate specificity[90]. The large hydrophobic S1 accessory pocket, hosting the rest of the substrate, is far more promiscuous allowing for binding of both folate and NAAG[91].

To better understand probe-protein interactions, in silico docking studies were performed between the two GUL radiolabels and a computationally-relaxed PSMA protein (PDB: 2XEG) [89]. Although the ligands' conformations differ (Figure 7c-d), both share similar interactions with the same Tyr552 (Y552) active site residue and the Zn atoms (Figure 8b) but F-GUL does not extend into the S1′ site like Ga-GUL does.

Both probes are predicted to have high affinity for PSMA, with induced fit docking scores around −15 kcal/mol (Table 3). Computed binding modes are consistent with the previously hypothesized interactions[90, 92, 93].

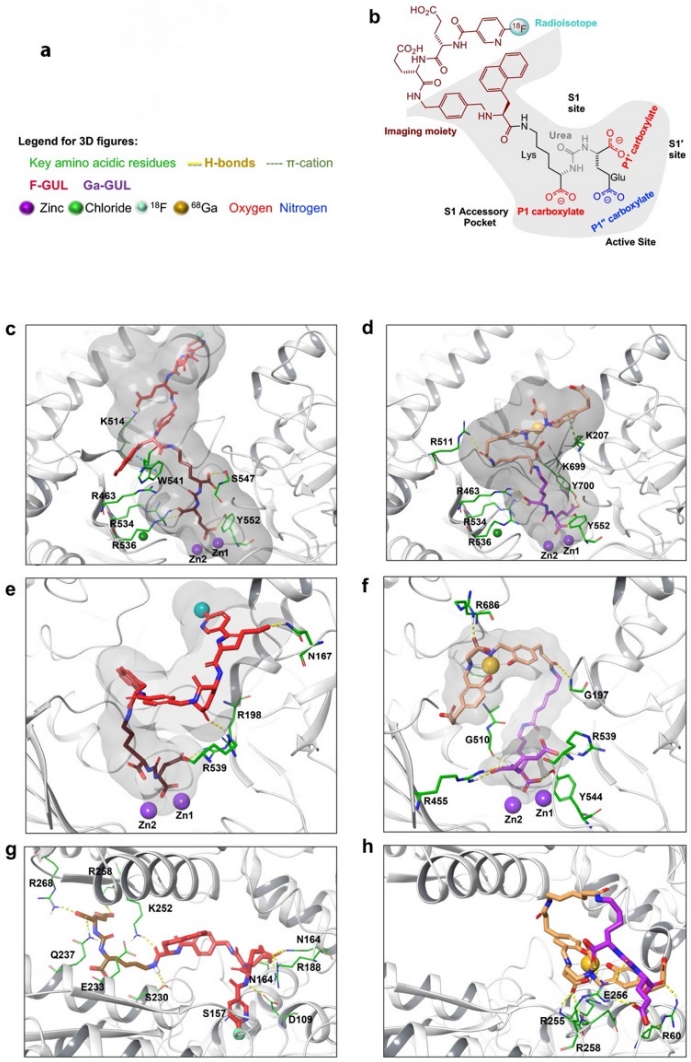

Figure 7 Structure of clinical PSMA probes and their binding modes within the PSMA, NAALADaseL and mGlur8 active sites.
(a) Legends for 3D panels. (b) F-GUL within the PSMA active site, showing the different regions of the active site and the substructure nomenclature of the probe. Computational modelling of (c) F-GUL and (d) Ga-GUL within the PSMA active site (*2XEG*), (e) F-GUL and (f) Ga-GUL within the NAALADaseL active site (*4TWE*) and (g) F-GUL and (h) Ga-GUL within the mGlur8 active site (*6BSZ*). The imaging moieties are shown in red (F-GUL) and beige (Ga-GUL) with the GUL moiety in brown (F-GUL) and purple (Ga-GUL). Key residues which form strong interactions—H-bonds (yellow dashed lines), π-cation (green dashed line)—are highlighted in green; and zinc, chlorine, gallium and fluorine atoms are spheres coloured purple, green, blue and orange respectively.

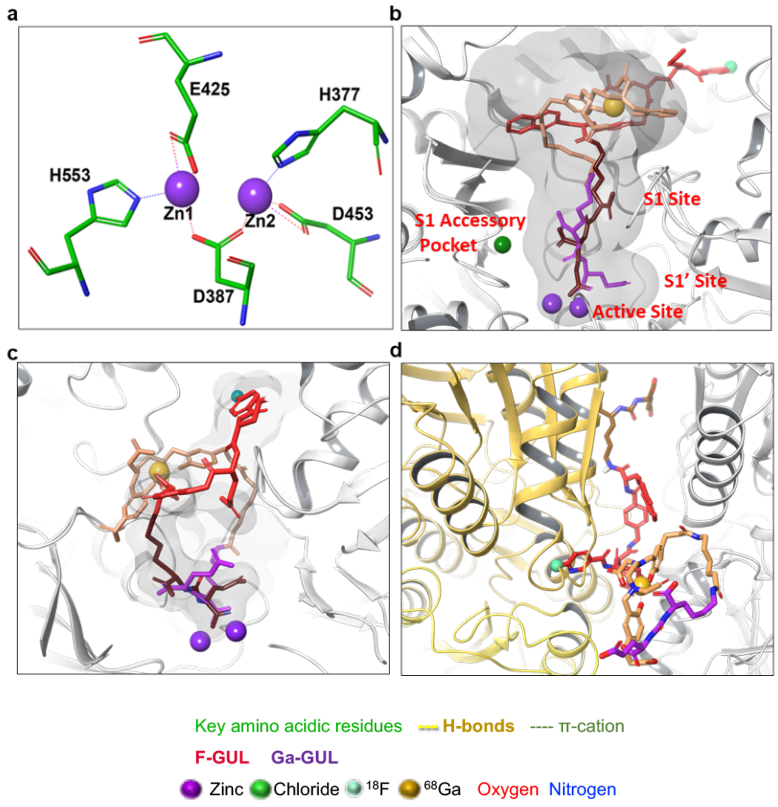

Figure 8 Zinc-binding in the PSMA active site. PSMA hosts two Zn2+ ions, responsible for substrate cleavage in its active site through shared coordination with five basic residues.
(a) Zinc ions in the PSMA active site are coordinated by five basic residues. Computational modelling of F-GUL (red and brown) and Ga-GUL (beige and purple) in (b) the PSMA active site (2XEG), with the active site-adjacent pockets labelled, (c) NAALADaseL active site (4TWE) and (d) mGluR8 within the dimer cleft (6BSZ).

Table 3 Docking scores for the probes with the target proteins from both rigid and induced docking models (kcal/mol).

Receptor	Ligand	Docking Score (kcal/mol)	
		RRD Score	IFD Score
PSMA	Cy3-GUL	−12.93	−13.73
	Ga-GUL	−11.29	−13.10
	F-GUL	−11.66	−14.83
NAALADaseL	Cy3-GUL	−9.09	−10.83
	Ga-GUL	−1.69	−12.25
	F-GUL	−8.20	−12.91
mGluR8	Cy3-GUL	−8.15	−11.28
	Ga-GUL	−4.09	−6.64
	F-GUL	−7.67	−13.16

The P1″ glutamate carboxylate moiety of F-GUL (Figure 7) forms strong interactions with the zincs (2.06 Å and 1.95 Å), and a strong hydrogen bond (2.06 Å) to the phenolic H of the S1′ Tyr552. A major structural feature of PSMA's S1 site is the "accessory pocket," whose entrance lid comprises three arginine residues (Arg536, Arg534, and Arg463) that can flip open to accommodate larger molecules. The P1′ carboxylate of F GUL is stabilized by H-bonds with these residues Arg536 (1.73 Å) and Arg534 (1.67 Å); while the P1 carboxylate has a strong H-bond interaction with nearby Ser547. The rigidity of the F GUL linker enables the radiolabel-bearing moiety to remain inside the pocket. This results in a likely important π- π interaction with Trp541 and several H-bonds with Lys514 (Figure 9a).

Ga-GUL's longer nine-atom linker enables it to enter deeper, properly occupying the S1′ pocket (Figure 7d), engaging in H-bonds with Lys699 (1.81 Å) and Tyr700 (1.85 Å) through the P1″ acid, and Tyr552 (1.70 Å) through the P1′ acid. The P1 glutamate carboxylate forms an isosceles triangle interaction with 2.18 Å distances to both zinc ions. Ga-GUL's long linker forms H-bonds with Arg511 and a key π-cation interaction with Lys207 that guides the probe into place (Figure 9b).

This structural tour, consistent with the literature,[94] gave us confidence in the binding mode of the probes. Consequently, we extended this approach to the two NEPC-suspect proteins.

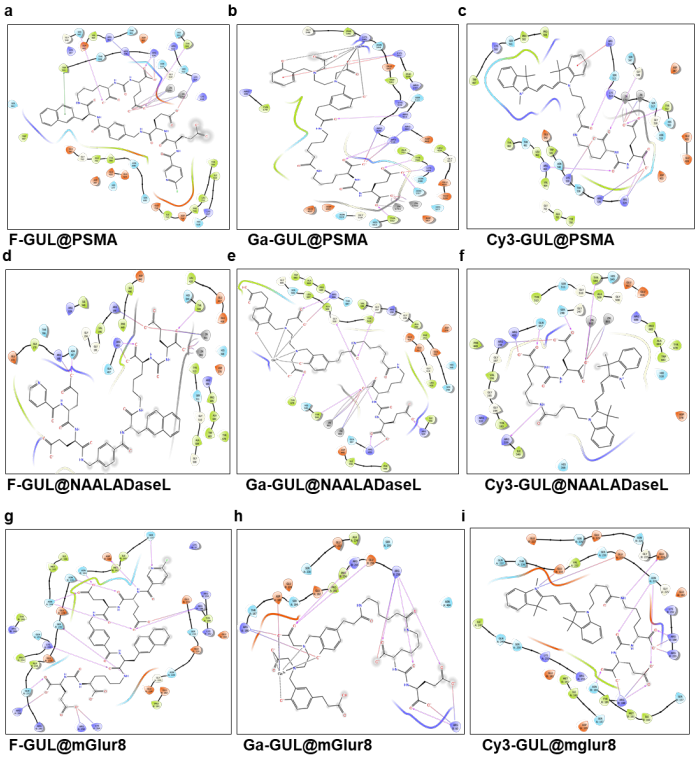

Figure 9 Ligand interaction diagrams of the three probes with the three proteins.
Ligand interaction diagrams highlight the dominant non-covalent interactions between the top docked pose for each of the three ligands in complex with (a-c) PSMA (*2XEG*), (d-f) NAALADaseL (*4TWE*) and (g-i) mGluR8 (*6BSZ*).

3.2. F-GUL and Ga-GUL bind NAALADaseL1 and mGLuR8.

F-GUL's GUL moiety binds to NAALADaseL1 in a manner reminiscent of **Ga-GUL**'s PSMA binding, occupying the S1′ pocket due to NAALADaseL1's larger, more open pocket (Figure 7**e**). **F-GUL**'s P1″ glutamate carboxylate forms an H-bond with Arg198, while the P1′ carboxylate bridges $Zn(1)^{2+}$ and $Zn(2)^{2+}$ at distances of 2.07 Å and 2.27 Å, respectively. **F-GUL**'s aromatic domains are positioned on the outer surface of the receptor, stabilized by a series of H-bond interactions with Asn167 and Arg539 (Figure 9**d**). The carboxylates of **Ga-GUL**'s glutamates adopt analogous positions (Figure 7**f**), but the linker takes a very different path out of the active site through the wide channel (Figure 8**c**); Arg539–P1″ carboxylate, Arg455–P1′ carboxylate and Gly510–ureido carbonyl H-bonds hold the linker in conformation. The **Ga-GUL** P1′ carboxylate interacts with $Zn(1)^{2+}$ and $Zn(2)^{2+}$ at distances of 2.17 Å and 2.09 Å, respectively (Figure 9**e**). The subtly different structure clearly induces differences in conformation (Figure 8**c**), but docking scores predict both ligands to be excellent partners for the accommodating NAALADaseL1 (**Table 3**).

The mGluRs always self-assemble into homodimers *in vivo*. The probes were docked (without restrictions) to each of the eight mGluR homodimers, but showed the best affinity for mGluR1, mGluR5 and mGluR8 (**Table 4**).

Table 4 Docking scores for both rigid and induced docking to mGluRs1-8 for the three probes.

Receptor	Ligand	Docking Score (kcal/mol)	
		RRD Score	**IFD Score**
mGluR1	Cy3-GUL	-6.06	-7.35
	Ga-GUL	-9.22	-10.70
	F-GUL	-6.66	-11.55
mGluR2	Cy3-GUL	−5.82	-7.879
	Ga-GUL	−7.81	-9.74
	F-GUL	−6.95	-9.51
mGluR3	Cy3-GUL	-5.13	-5.73
	Ga-GUL	-6.09	-6.59
	F-GUL	-5.21	-8.25
mGluR4	Cy3-GUL	−5.82	-7.155
	Ga-GUL	−3.83	−5.21
	F-GUL	−7.76	−8.80
mGluR5	Cy3-GUL	-4.1	-9.11
	Ga-GUL	-8.05	-11.43
	F-GUL	-10.12	-11.09
mGluR6	Cy3-GUL	-5.46	-7.18
	Ga-GUL	-5.15	-9.38
	F-GUL	-5.460	-10.96
mGluR7	Cy3-GUL	-6.31	-8.01
	Ga-GUL	-8.62	-8.89
	F-GUL	-6.53	-8.97
mGluR8	Cy3-GUL	−8.15	−11.28
	Ga-GUL	−4.09	−6.64
	F-GUL	−7.67	−13.16

Curiously, the probes do not interact with the glutamate-binding active site of these proteins, which is far narrower than either PSMA's or NAALADaseL1's; instead, they bind to the large inter-monomer cleft (Figure 7**g-h**). Induced-fit docking predicts the best binding to mGluR5 and 8, with scores on par with NAALADaseL1 and only slightly inferior to PSMA (**Tables 3** and **4**). The docking scores to the other mGluRs were lower (−5.2 to −13.2) but remain favourable. Molecular dynamics simulations helped us understand the high docking score and the unusual binding mode of the probes with mGluR8, which we identified as being particularly NEPC relevant (*vide infra*). Very little movement is observed within the binding cleft for either ligand: most structures fall within a 1 Å cluster (Figure 22) due to an extensive hydrogen bonding network that forms between the positively charged residues of the cleft and the negatively charged probes (Figure 10-21).

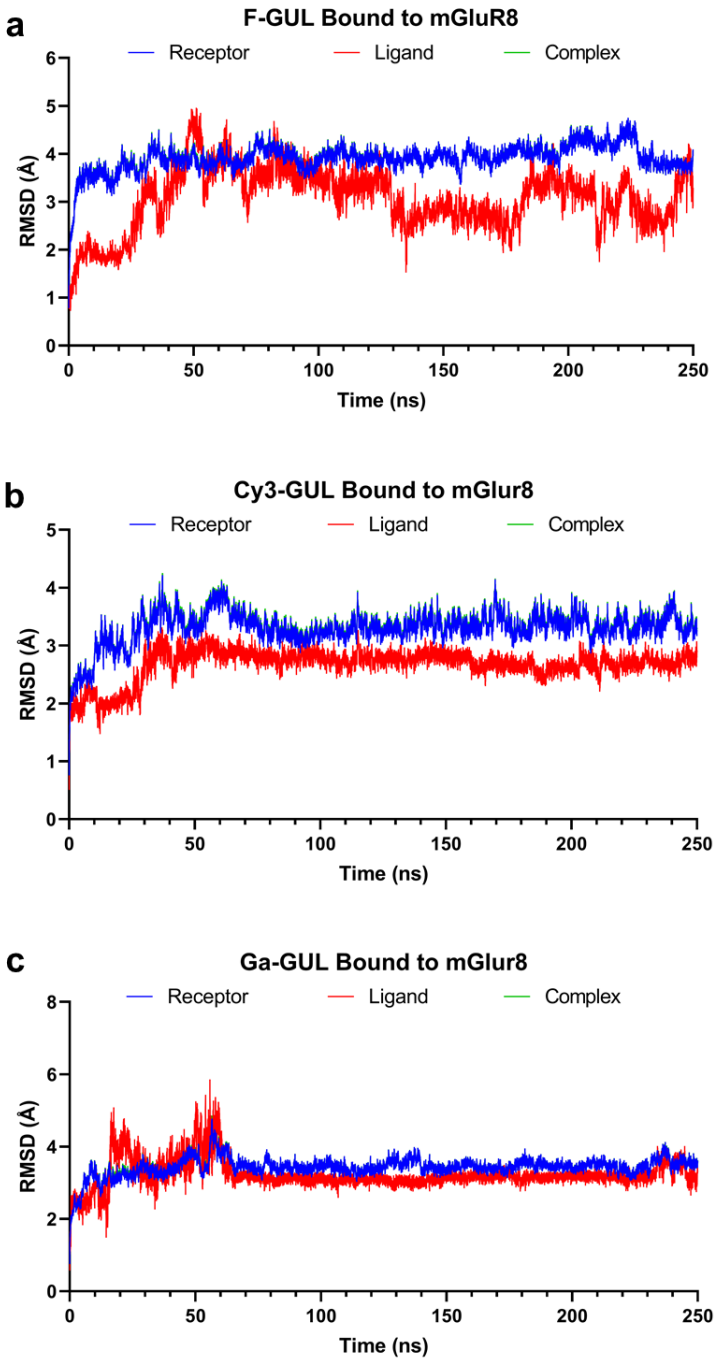

Figure 10 mGluR8 RMSD (Å) over a 250 ns MD simulation F-GUL (a), Cy3-GUL (b) and Ga-GUL (c) bound to mGluR8.

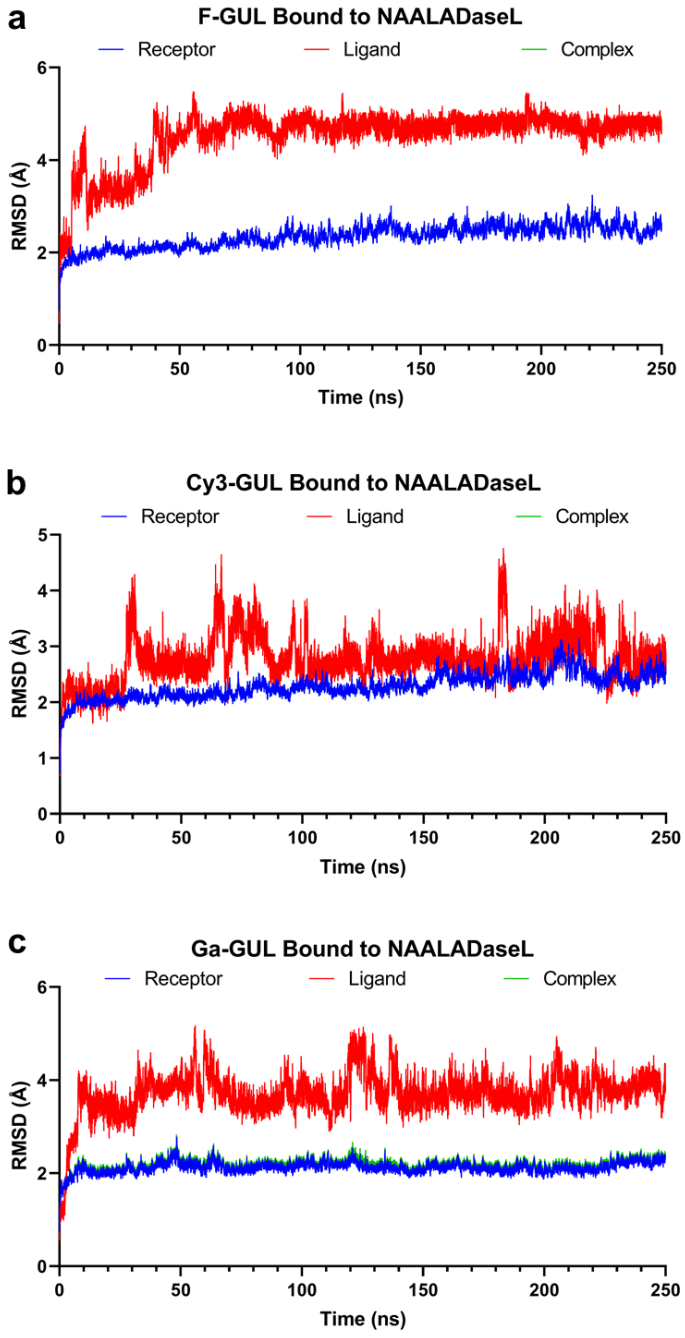

Figure 11 NAALADaseL1 RMSD (Å) over a 250 ns MD simulation F-GUL (a), Cy3-GUL (b) and Ga-GUL (c) bound to NAALDaseL.

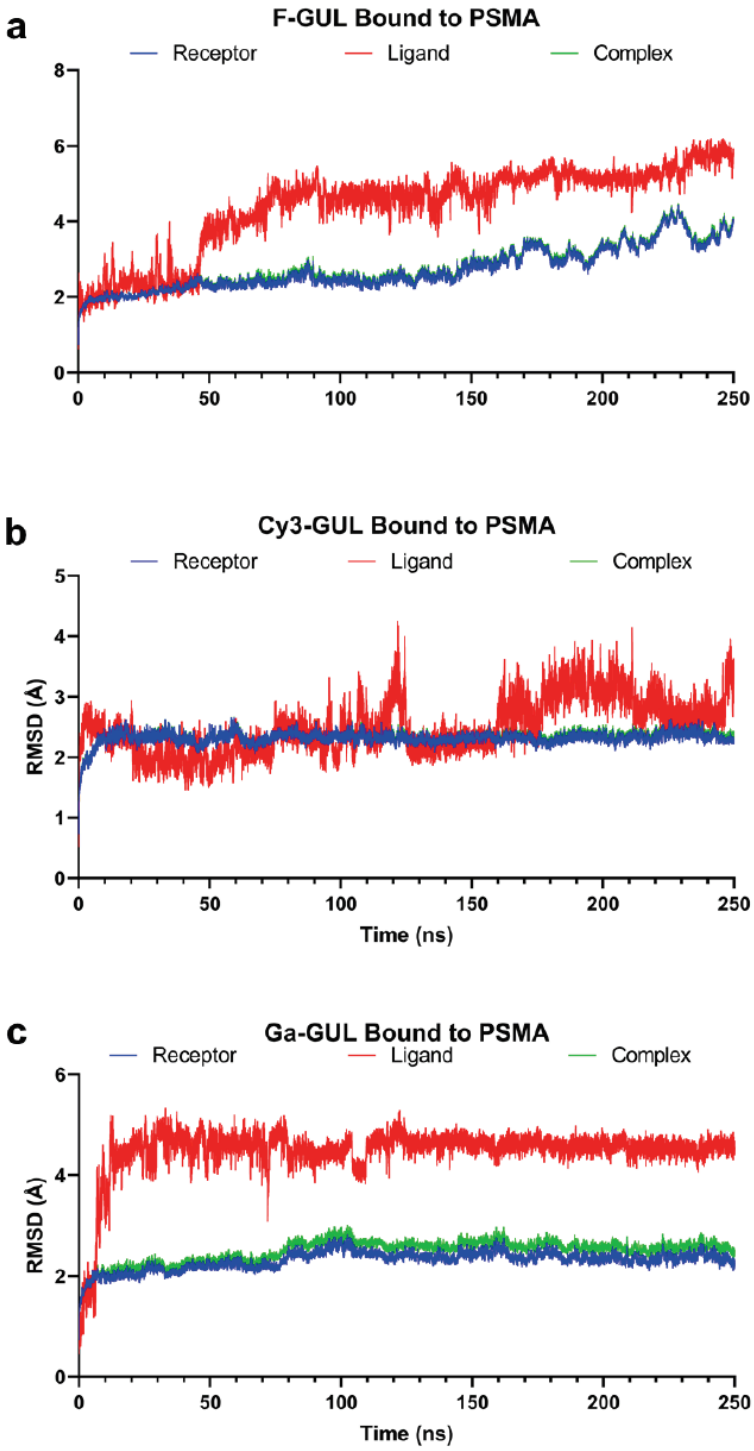

Figure 12 PSMA RMSD (Å) over a 250 ns MD simulation F-GUL (a), Cy3-GUL (b) and Ga-GUL (c) bound to PSMA.

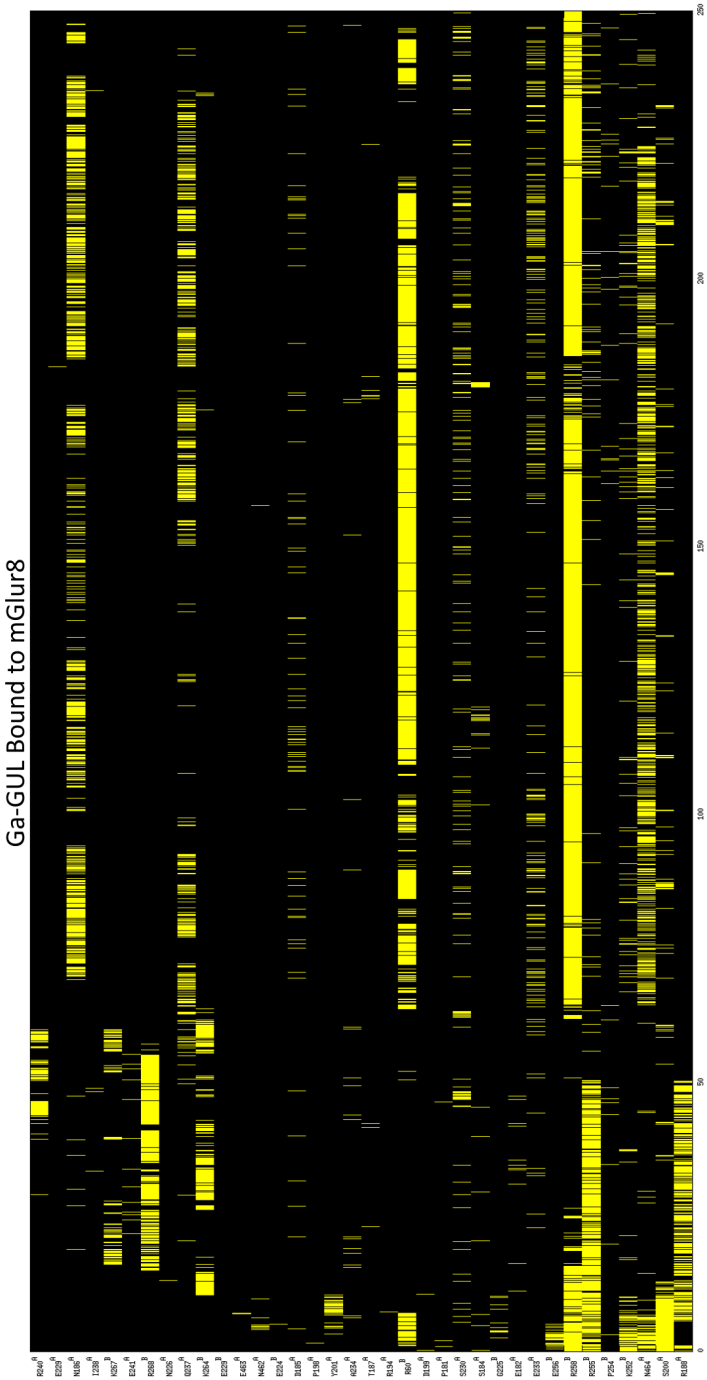

Figure 13 Hydrogen binding interactions of Ga -GUL with mGluR8 over a 250 ns MD simulation.

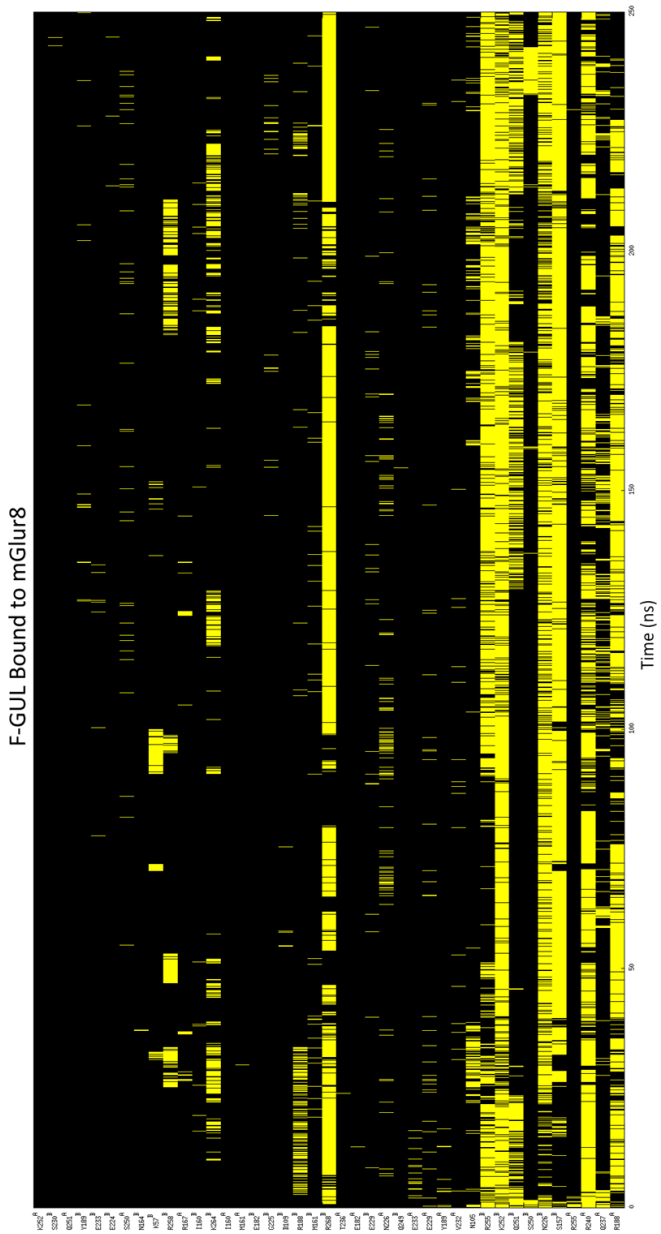

Figure 14 Hydrogen binding interactions of F-GUL with mGluR8 over a 250 ns MD simulation.

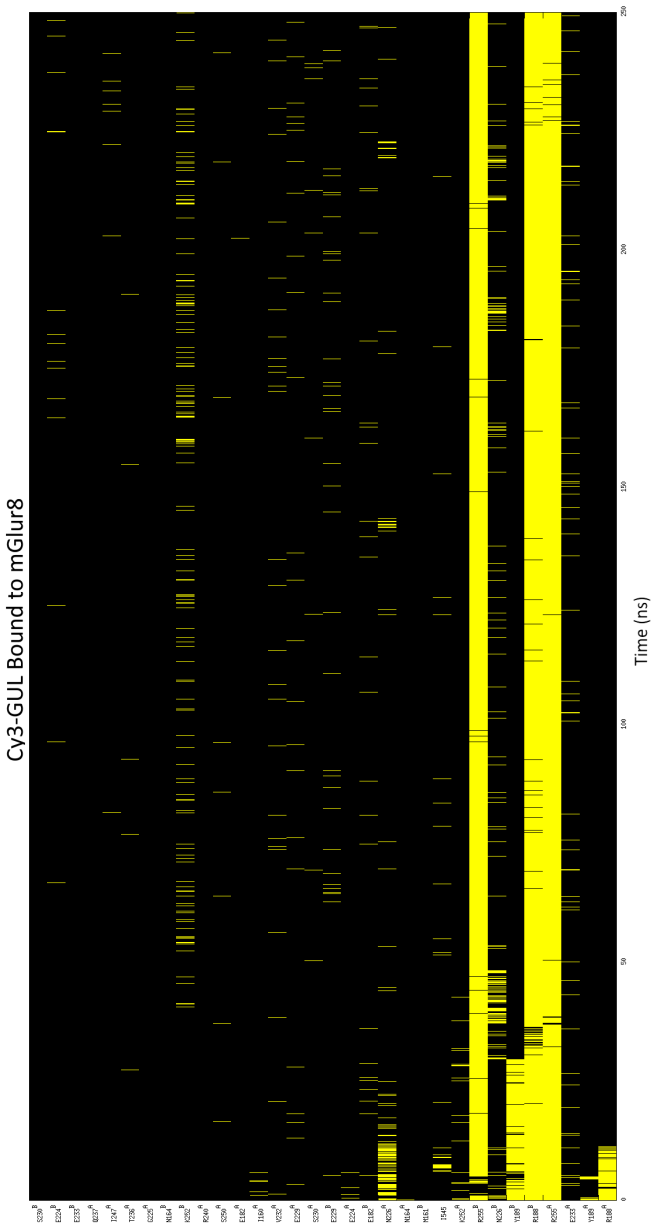

Figure 15 Hydrogen binding interactions of Cy3-GUL with mGluR8 over a 250 ns MD simulation.

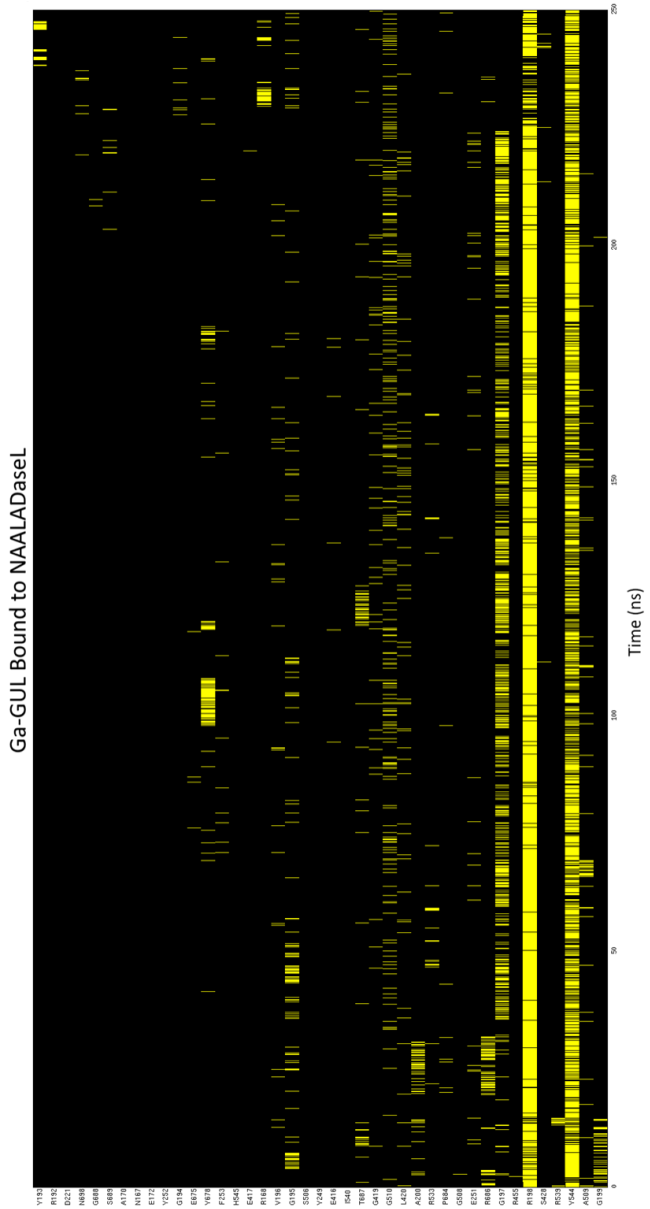

Figure 16 Hydrogen binding interactions of Ga-GUL with NAALADaseL over a 250 ns MD simulation.

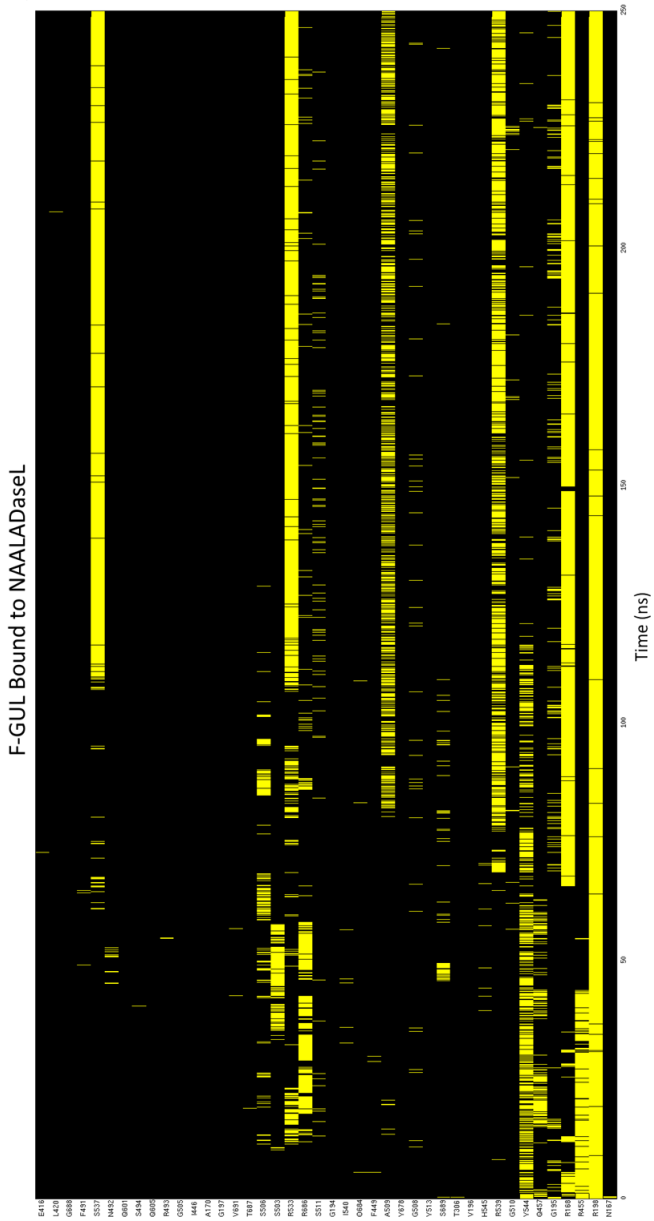

Figure 17 Hydrogen binding interactions of F-GUL with NAALADaseL over a 250 ns MD simulation.

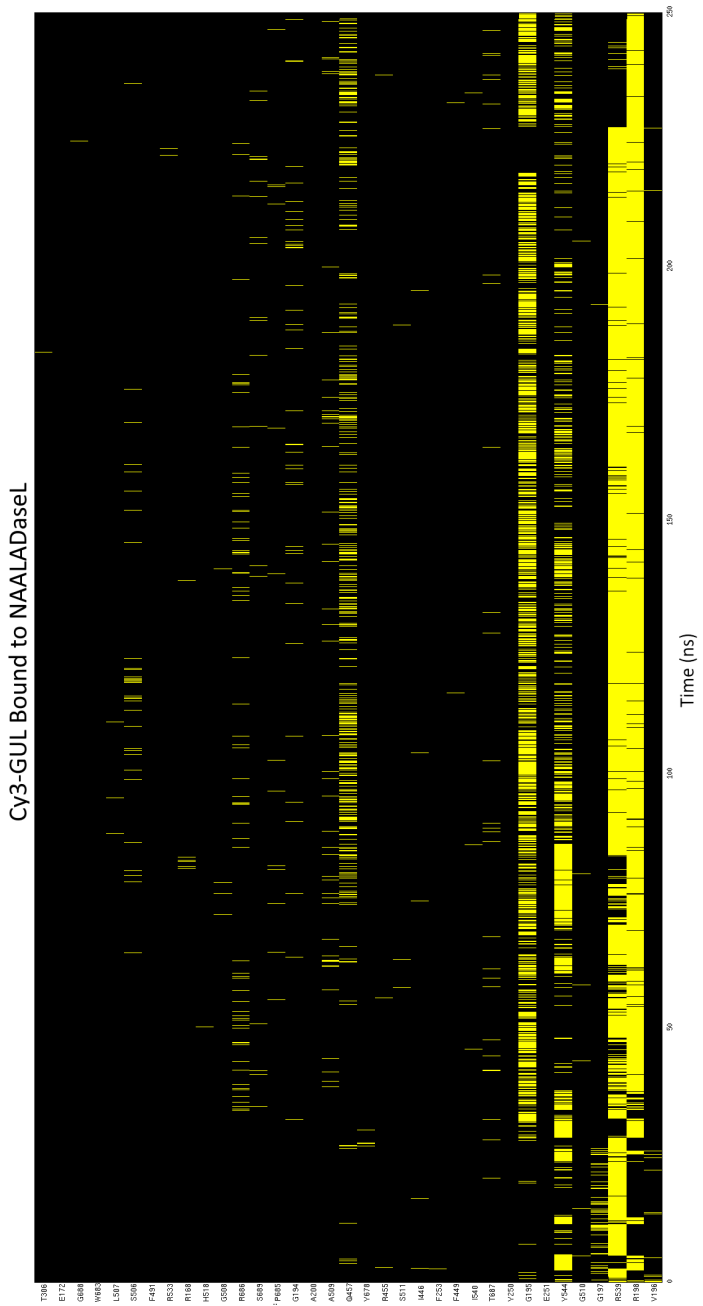

Figure 18 Hydrogen binding interactions of Cy3-GUL with NAALADaseL over a 250 ns MD simulation

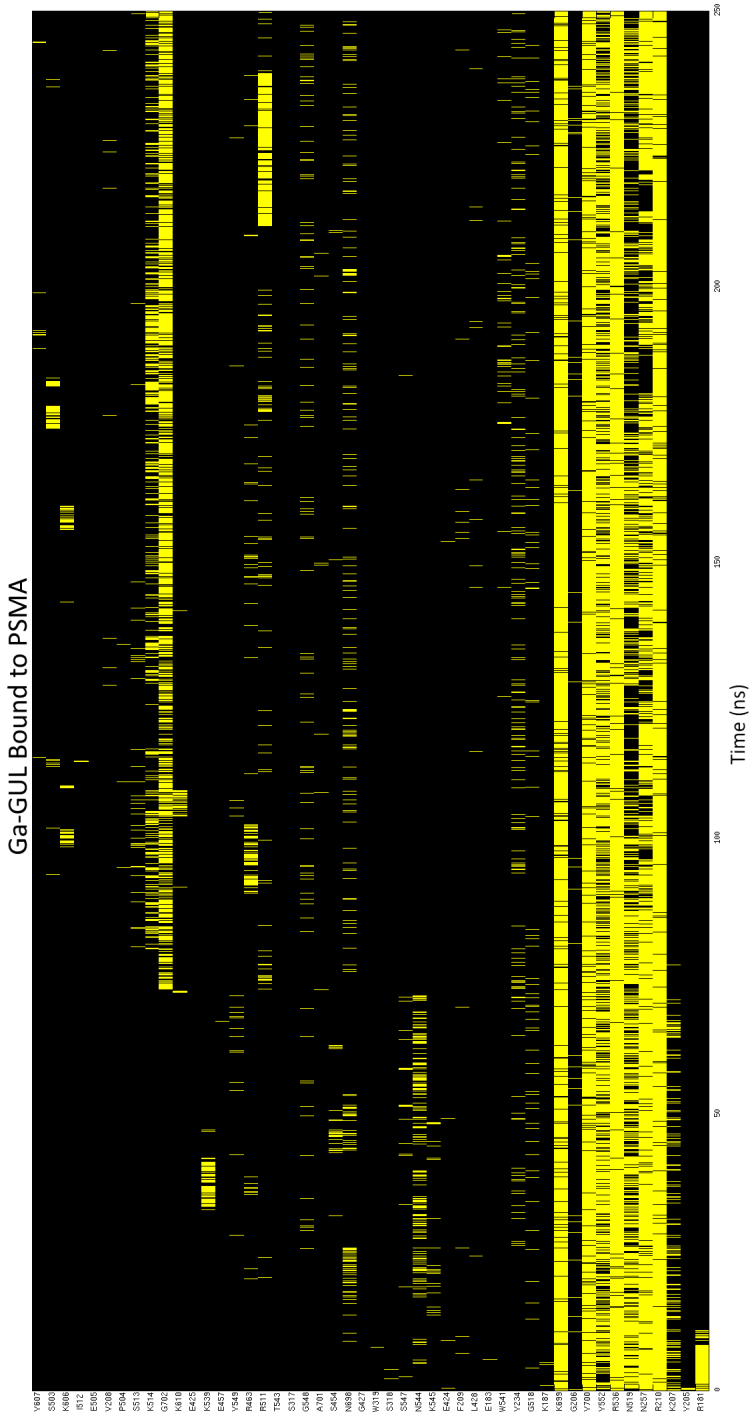

Figure 19 Hydrogen binding interactions of Ga-GUL with PSMA over a 250 ns MD simulation.

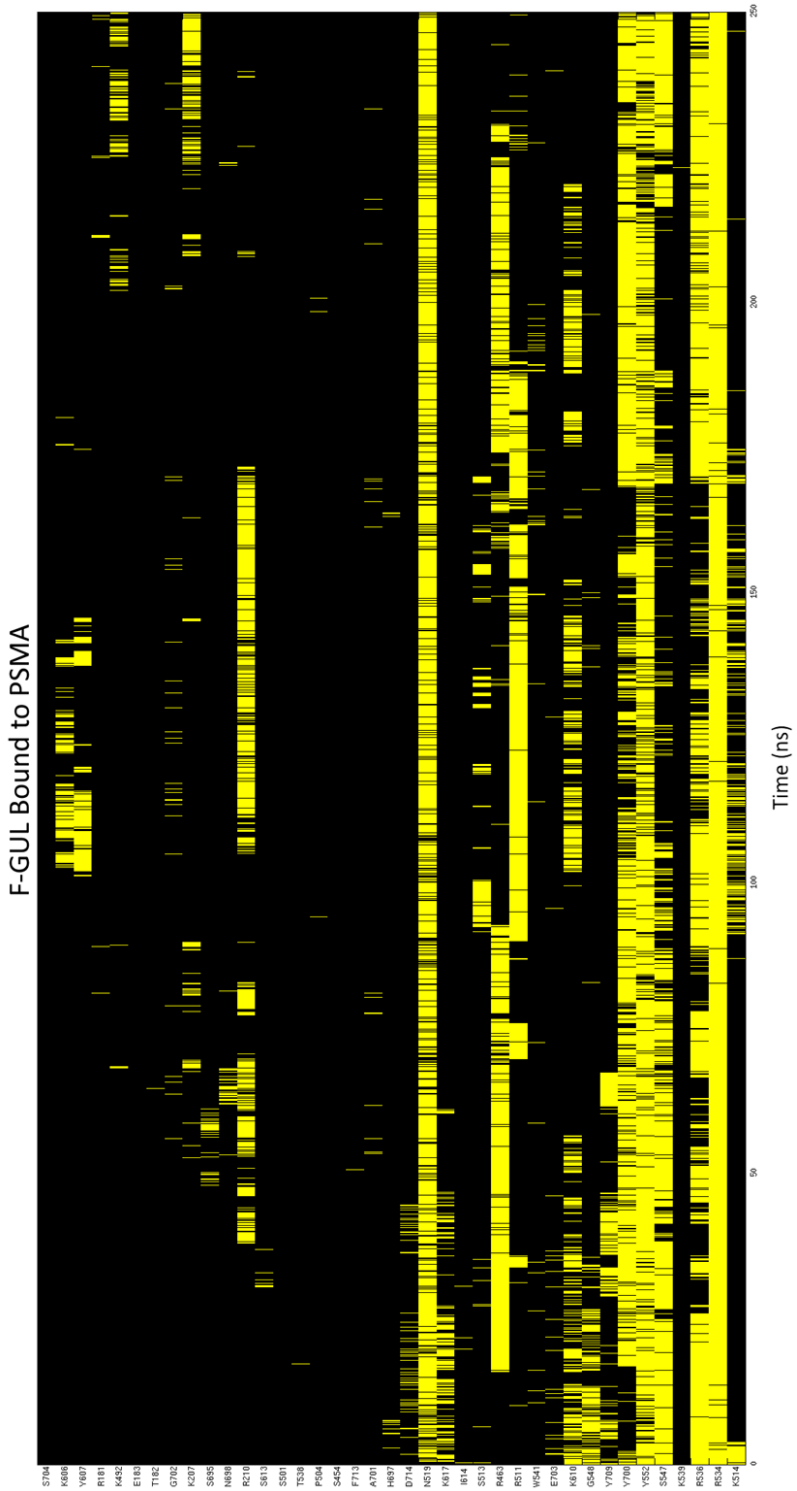

Figure 20 Hydrogen binding interactions of F-GUL with PSMA over 250 ns MD simulation.

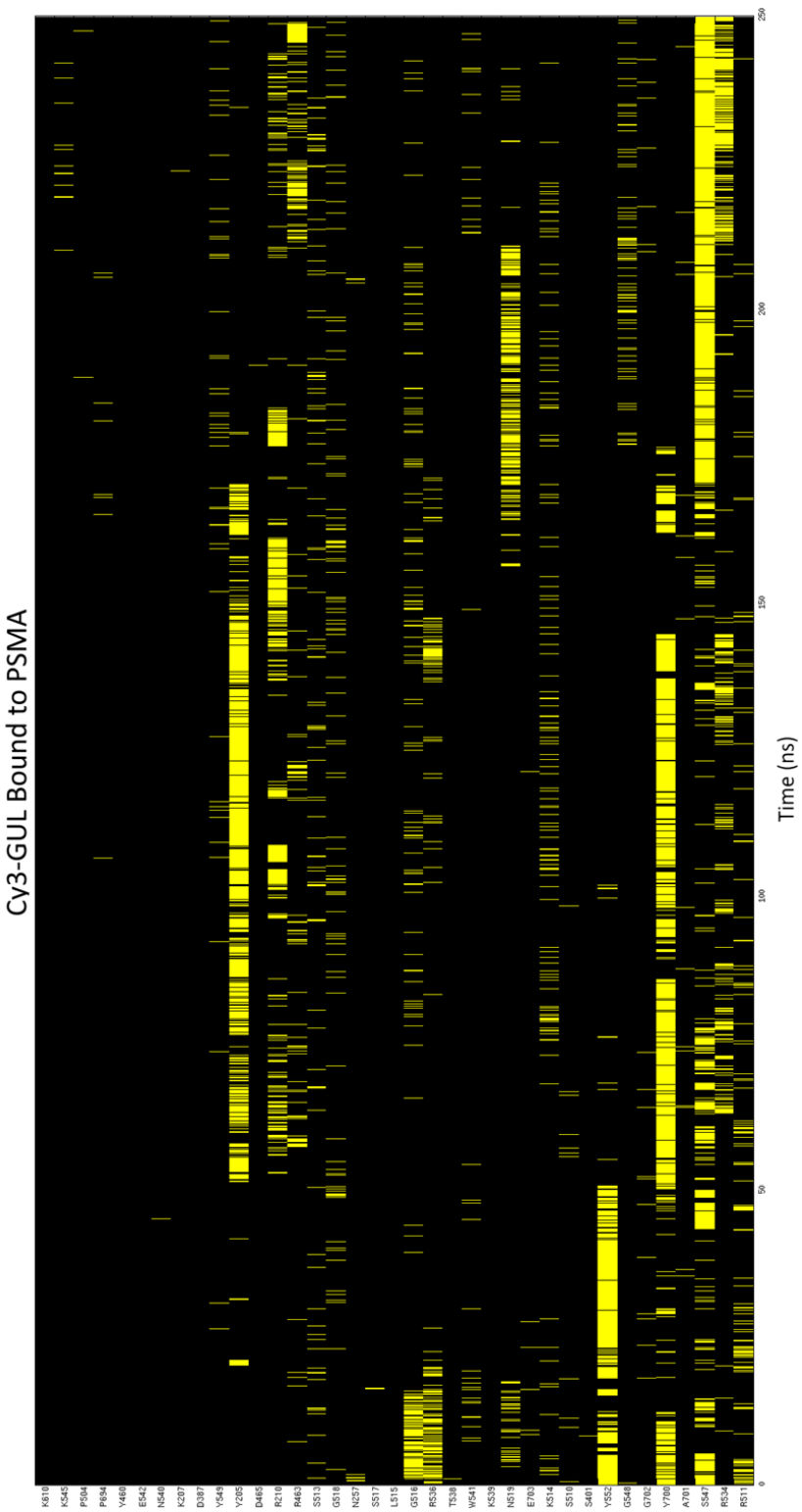

Figure 21 Hydrogen binding interactions of Cy3-GUL with PSMA over a 250 ns MD simulation.

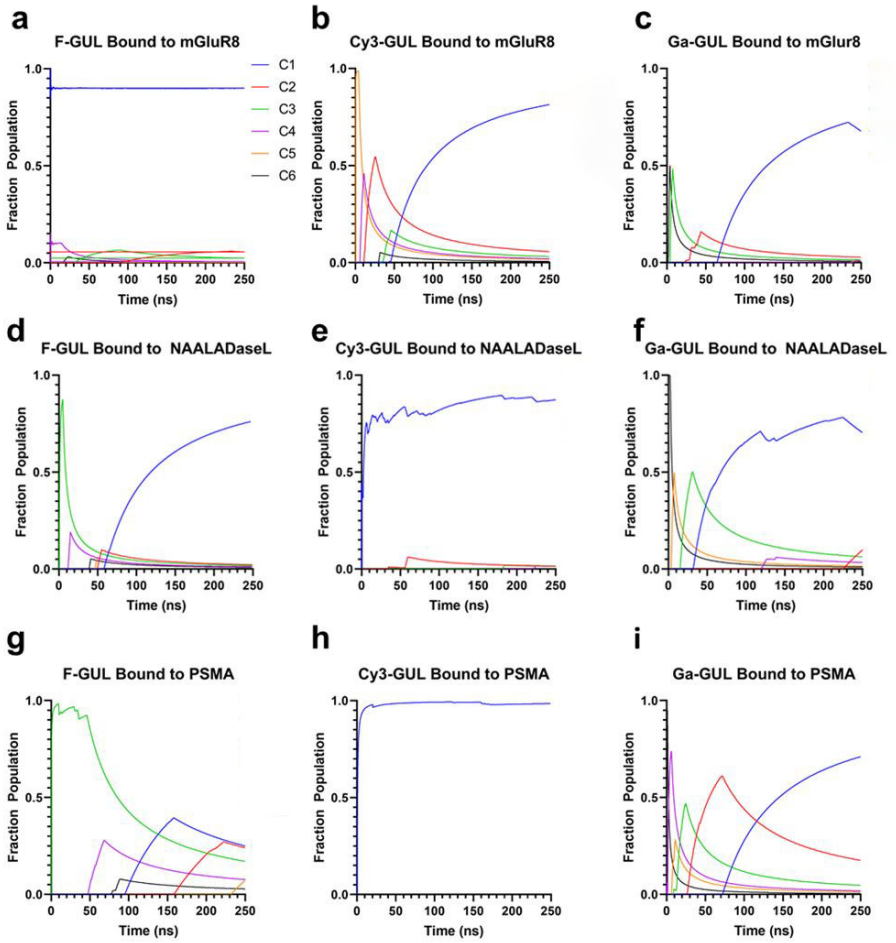

Figure 22 Relative populations of protein-ligand conformations. MD simulation and the relative populations of the clusters of the three probes (F-GUL, Cy3-GUL and Ga-GUL) bound to mGluR8 (a-c), NAALDaseL (d-f) and PSMA (g-i) over 250 ns MD simulation.

However, the two probes bind very differently despite both having strong affinity (Figure 8**d**), possible due to the large size of the cleft. **F-GUL** (Figure 7**g**) is particularly stable, adopting an extended conformation maximizing hydrogen bonding interactions between the glutamate and the highly positive interprotein region's residues Arg188, Arg240 of one monomer, and Ser157, Asn226, Lys252, Arg255, and Arg268 in the other (Figure 9**g**). **Ga-GUL** (Figure 7**h**) forms far fewer interactions and instead folds in on itself, held together by an intramolecular hydrogen bond; but it still interacts with Ser200, Gln237, Asn186, of one monomer and Arg60 and Arg255 in the other. Both complexes are highly stabilized through these interactions making mGluR8 an exceptional potential molecular target (Figure 9**h**).

These data predict that both **F-GUL** and **Ga-GUL** will have strong affinity, comparable to PSMA, for both NAALADaseL1 and a subset of mGluRs. It is conceivable that these two protein classes are responsible for the GUL probes' efficacy in detecting PSMA-suppressed cancers; however, it is unknown whether these proteins are associated with NEPC.

3.3. Aminopeptidase NAALADaseL1 is elevated in NEPC.

NAALADaseL1, encoded by *NAALADL1*, has high sequence similarity to PSMA (Figure 23**)**.[95] They share more than 90% structurally equivalent residues, with near complete identity at the active site (**Figure 23**, PDB: *2XEJ* and *4TWE*).[77]

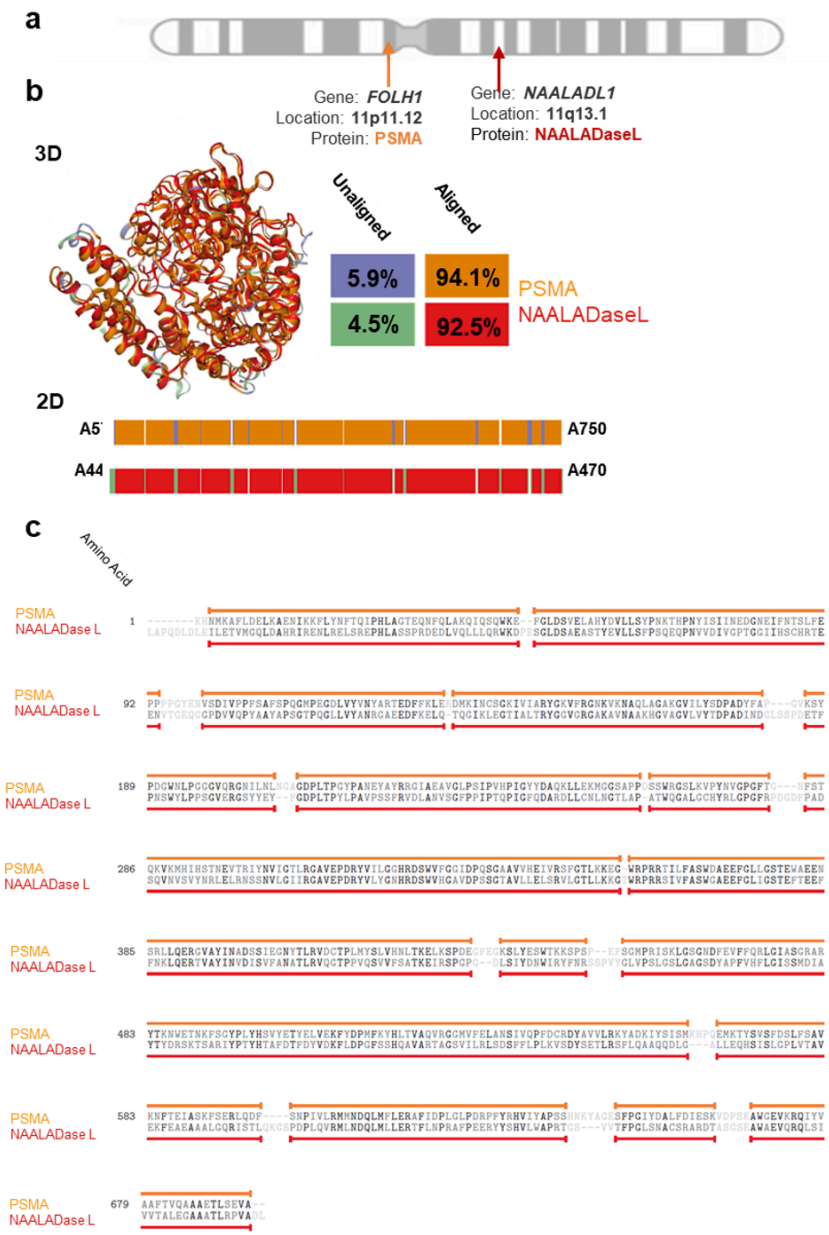

Figure 23 PSMA-like protein aminopeptidase NAALADaseL could be an alternative target for GUL-ligands.
(a), a schematic of the location of *FOLH1* and *NAALADL1* genes on human chromosome 11. (b), the pairwise structure comparison of PSMA (2XEJ) and NAALADaseL (4TWE) to generate the 2D and 3D alignment using the TopMatch portal. (c) The demonstration of the sequence similarity of PSMA and NAALADaseL. The pairwise structure sequences of PSMA (2XEJ) and NAALADaseL (4TWE) amino acids using the TopMatch portal. The structurally equivalent residues are shown in bold if they are the same amino acid.

We examined the expression of NAALADaseL1 using the LTL331 patient-derived xenograft model of prostate cancer progression from adenocarcinoma-to-NEPC (Figure 24**a**).[71] *NAALADL1* gene expression remains minimal during the effective treatment period, but spikes as the tumour becomes resistant to therapy and peak expression occurs when the tumour transitions to NEPC. This profile inversely correlates with that of *FOLH1* (Figure 24**a)**. This trend is mirrored in the Dream Team patient dataset (Figure 24**b**);[96] when ordering patients by increasing AR expression, *NAALADL1* expression falls while PSMA expression increases; furthermore, NEPC score is strongly positively correlated with *NAALADL1* expression. As NAALADaseL1 is elevated in low-PSMA prostate cancers with an NEPC gene signature (**Figure 24c-d**), this data supports the computational supposition that NAALADaseL1 may be one target of the GUL probes on PSMA-suppressed cells.

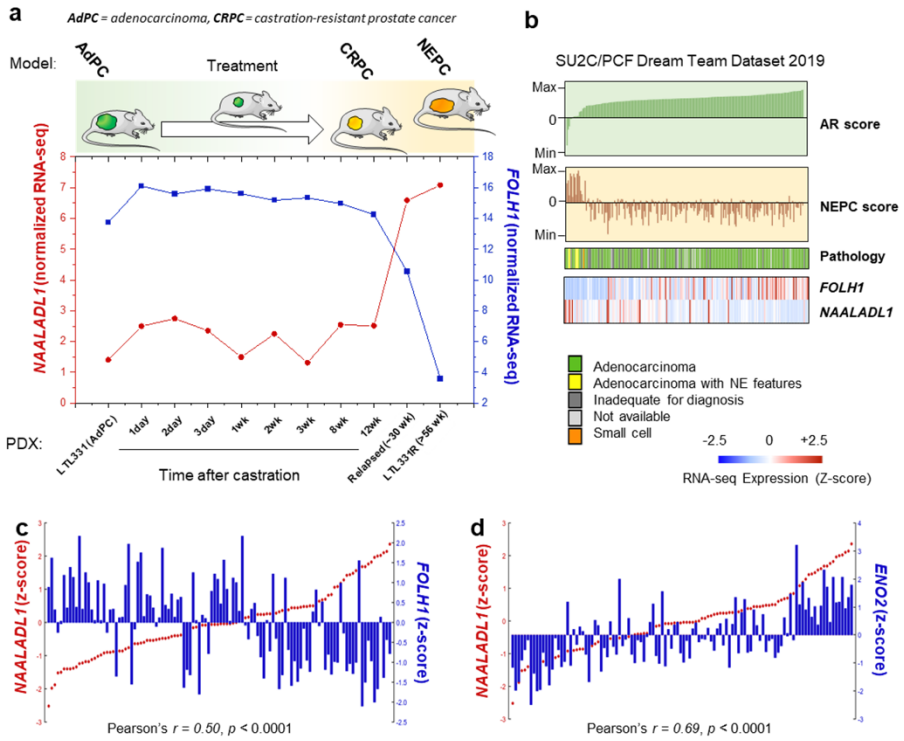

Figure 24 Differential expression of NAALADL1 in NEPC as an alternative target for GUL-ligands.

(a) Schematic of our established PDX mice models of adenocarcinoma prostate cancer (AdPC) and NEPC, and alteration of *FOLH1* and *NAALADL1* gene expression during the transition from AdPC to NEPC; (b) Evaluation of the expression of FOLH1 and *NAALADL1* genes and their association with AR and NEPC scores in the SU2C/PCF Dream Team Dataset 2019.[96] The high levels of *NAALADL1* gene expression in AdPC is associated with both lower levels of *FOLH1* gene expression and higher levels of *ENO2* gene expression, the archetypal NE-marker; (c) Pearson's correlation between *FOLH1* (blue) and *NAALADL1* (red) expression levels; (d) Pearson's correlation between *ENO2* (blue) and *NAALADL1* (red) expression levels among AdPC samples (n = 199) generated by R2: Genomics Analysis and Visualization Platform (**http://r2.amc.nl**).

3.3. mGluRs are upregulated during progression to NEPC.

The second class of proteins identified for investigation were the mGluRs. While increased expression of mGluR2 has already been reported in PSMA-positive cancers,[44] we observed a significant upregulation in the expression of most mGluR family members during cancer progression from normal prostate adenocarcinoma (HSPC) to NEPC in our PDX mouse model (**Figure 25a-b**).

Following castration, *GRM 2, 3, 4* and *8* all become increasingly expressed as *FOLH1* downregulates. Furthermore, their expression is strongly positively correlated to that of *SRRM4*, which is the archetypal biomarker of NEPC (**Figure 26**). Data mining the Memorial Sloan Kettering Cancer Center cohort[97] for prostate tumor survival, identifies that high levels of *GRM1, 3, 4,* and especially *5* and *8* are correlated with shorter times to biochemical recurrence, with *GRM8* showing the most significant effect (**Figure 27**). Further investigation revealed that *GRM8* expression is low in both benign tumours and in localized hormone sensitive prostate cancer (HSPC), but it rises markedly in metastatic disease (**Figure 28)**.

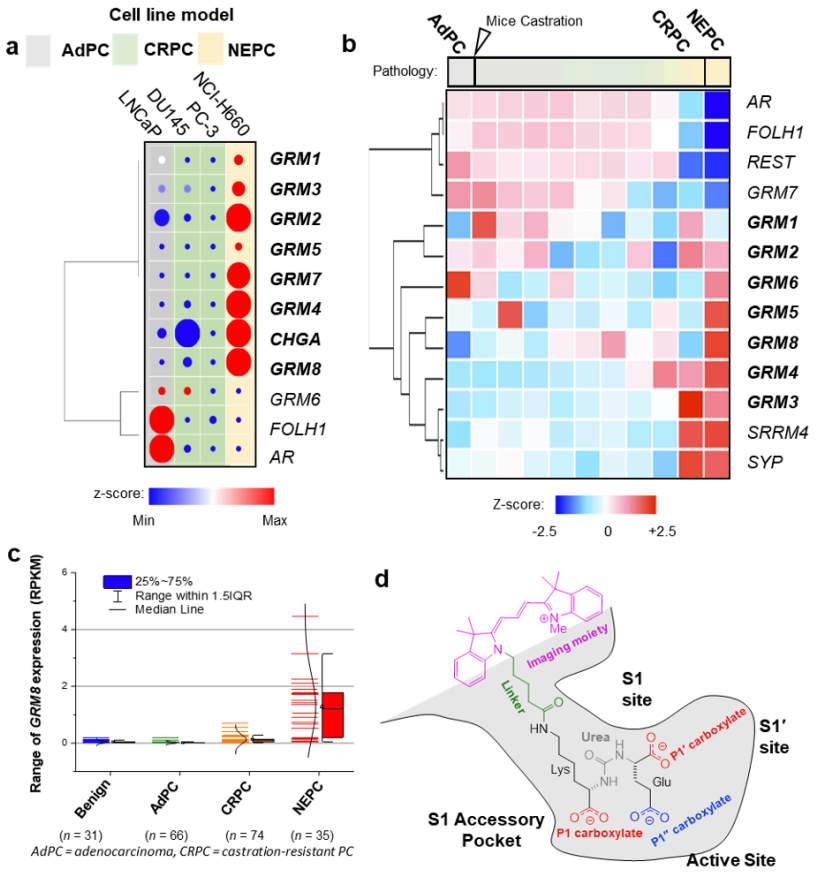

Figure 25 Differential expression of GRM genes is associated with higher expression of NEPC-markers and shorter times to biochemical relapse.
(a) The heatmap plot of the expression levels of GRMs levels in well-established AdPC cell lines defined as hormone-sensitive adenocarcinoma prostate cancer (grey), castration-resistant prostate cancer (green) and NEPC (yellow) (b) Transcription changes in the GRM genes during progression from AdPC to NEPC in a series of PDX mice models. (c) mGluR8 gene expression level in different cohorts of PC. (d) Structure of novel probe Cy3-GUL.

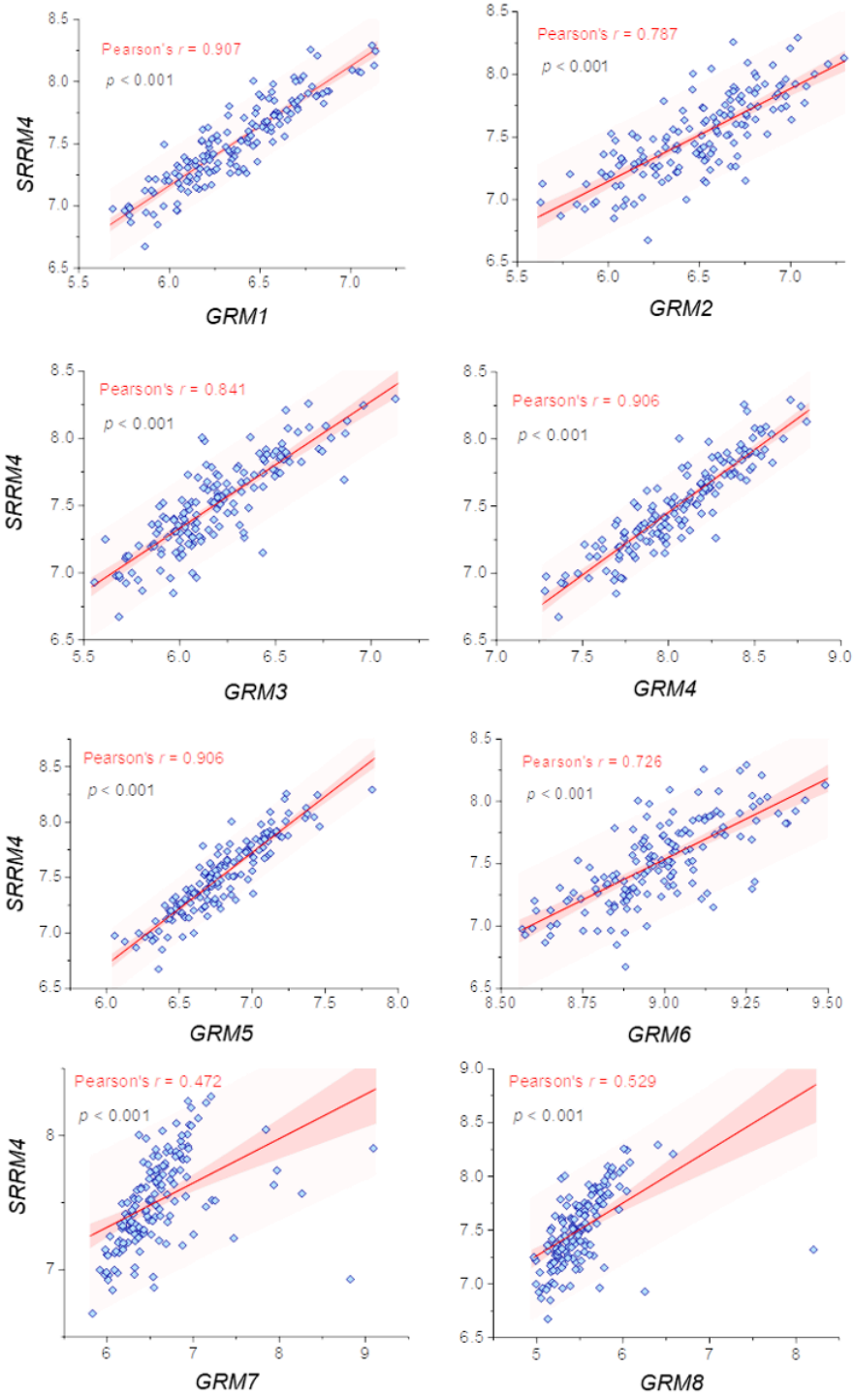

Figure 26 The relationship between *GRMs* and *SRRM4* levels in our PDX mouse model by Pearson correlation analysis.

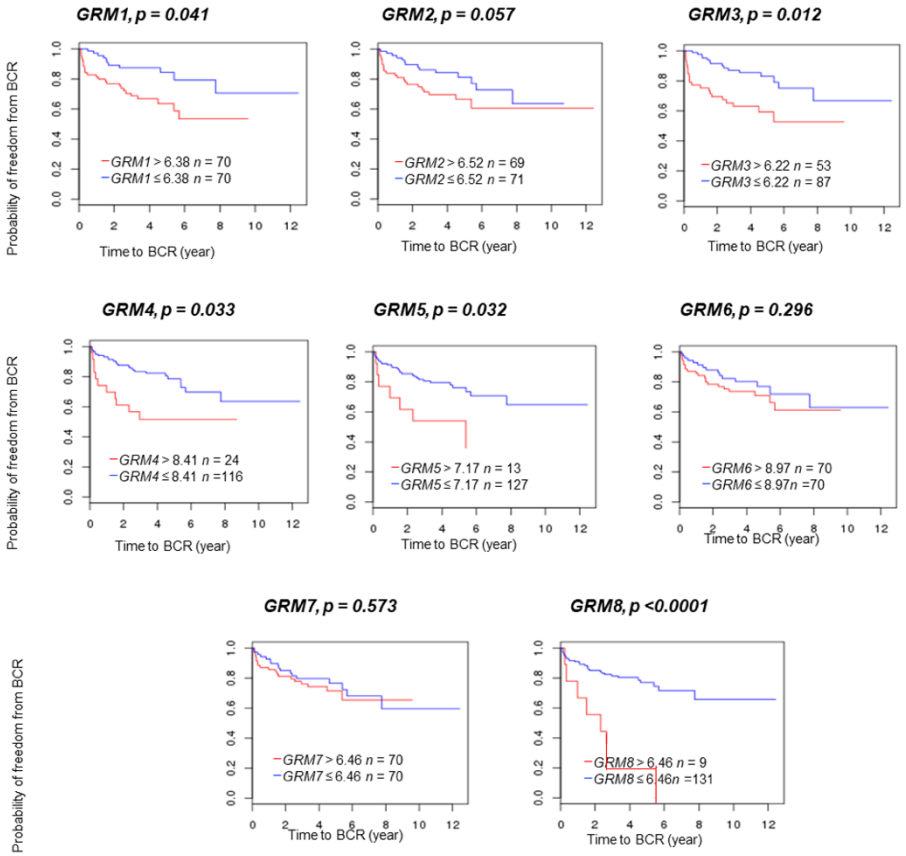

Figure 27 Kaplan-Meyer survival curves for high and low expression levels of GRMs. BCR; biochemical recurrence.
Data obtained from the Dream Team dataset.

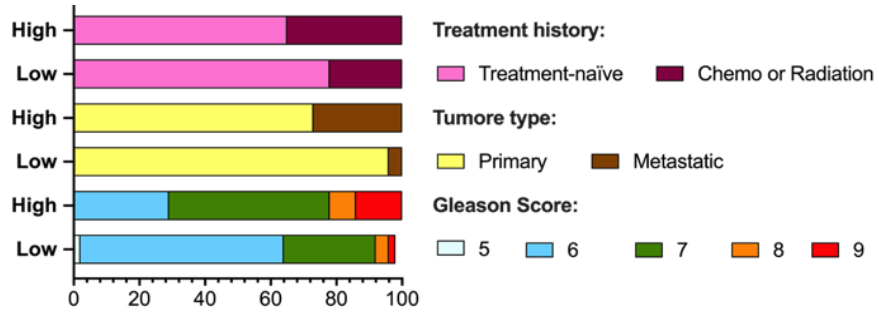

Figure 28 High GRM8 expression correlates with poor outcomes.

High levels of *GRM8* expression is associated with a higher prevalence of metastatic cancer, and higher Gleason score specimens. *GRM8* expression is pathologically confirmed in NEPC.

This analysis shows that its expression rises during the transition to castration-resistant prostate cancer and can be significantly elevated in histopathologically-confirmed NEPC (Figure 24**c**). The mGluRs are clearly associated with NEPC, and their molecular role deserves further attention and investigation. Together with NAALAD1, the biochemical and computational data all suggest that the GUL probes might have two proteins that can explain their binding to PSMA-suppressed cells.

3.4. A novel synthetic fluorescent Cy3-GUL probe is predicted to bind to all three proteins.

To validate this hypothesis, we analyzed our predicted binding modes of **F-GUL** and **Ga-GUL** to design a novel cyanine dye-incorporating fluorescent probe (**Cy3-GUL**, Figure 25**d**) analogue of the clinical radiolabels (Figure 29). A series of related probes with different linkers were computationally screened using docking, but the best binding results were observed for a synthetically simple analogue, **Cy3-GUL**, where a five-atom linker connects the GUL pharmacophore to the cyanine. This is a far closer connection than employed in either of the radiolabels but maintains the steric bulk at approximately the same distance from the GUL pharmacophore as **F-GUL**'s naphthylalanine.

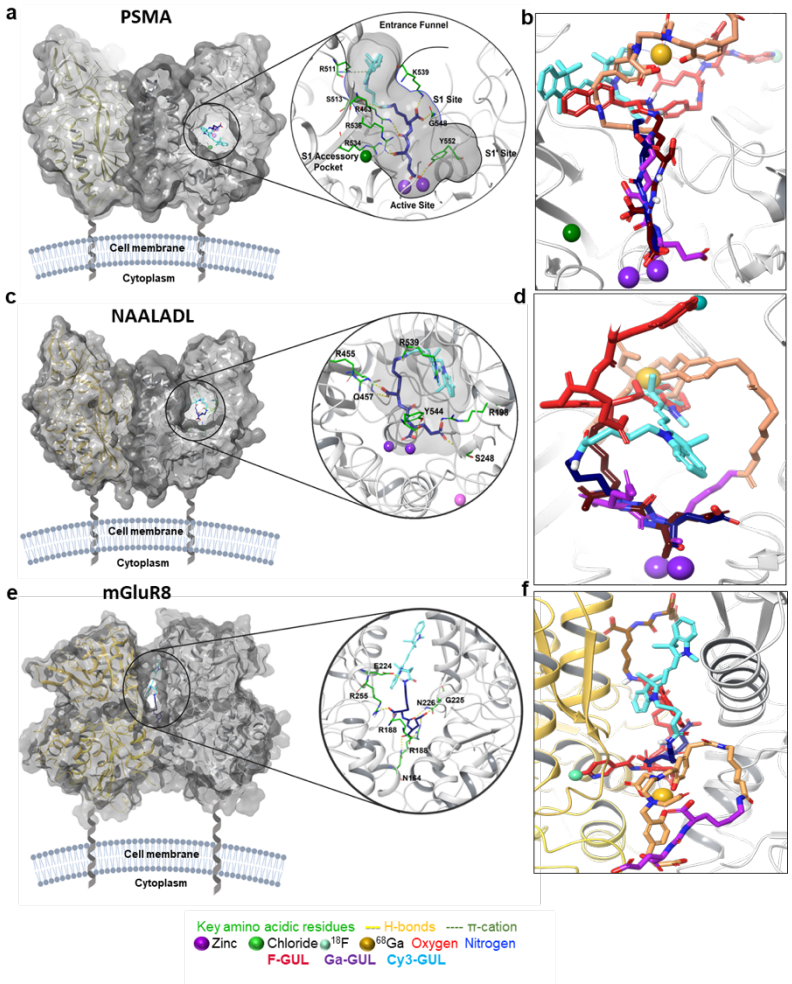

Figure 29 Novel probe Cy3-GUL binds to the PSMA and NAALADL1 active sites and mGluR8 cleft similar to the clinical radiopharmaceuticals.
(a) Cy3-GUL's computed conformation within the PSMA active site (*2XEG*). (b) Comparison of Cy3-GUL (GUL moiety in deep blue, dye in cyan); Ga-GUL (GUL moiety in maroon, ligand in red); and F-GUL (GUL moiety in purple, pseudopeptide in peach) within the PSMA active site; (c) Cy3-GUL's computed conformation within the NAALADL1 active site (*4TWE*). (d) Comparison of Cy3-GUL, Ga-GUL, and F-GUL in the NAALADL1 active site, colouring the same as in (b). (e) Cy3-GUL's computed conformation within the mGluR8 cleft (*6BSZ*). (f) Comparison of Cy3-GUL, Ga-GUL, and F-GUL in the mGluR8 cleft, colouring the same as in (b).

Comparing the predicted binding of **Cy3-GUL** with PSMA to that of **Ga-GUL** and **F-GUL** suggests that **Cy3-GUL** will adopt a similar pose to **F-GUL**, interacting with one of the Zn^{2+} ions through the P1″ carboxylate (Figure 29**a**). **Cy3-GUL** forms fewer and less consistent hydrogen bonding interactions than the other probes and, unlike **Ga-GUL**, but like **F-GUL,** it does not enter the S1′ pocket; it also lacks **F-GUL**'s highly charged imaging moiety preventing a series of cation-π interactions (Figure 9**c**). However, it does hydrogen bond to Arg534, Ser547, Tyr552 and Tyr700. As a result, greater RMSD fluctuations occur for **Cy3-GUL** during the MD simulation (Figure 22). Although more flexible, **Cy3-GUL** still forms enough key interactions to remain an excellent ligand for PSMA.

Cy3-GUL is predicted to bind very well to NAALADL1 with similar affinity as **F-GUL** and **Ga-GUL** (Figure 29**c** and **Table 3**). The binding modes of all three probes are different due to the greater size of the NAALADaseL1 active site; however, they all bind with the GUL moiety extended into the binding pocket (Figure 29**d**). In the case of **Cy3-GUL**, the P1″ carboxylate forms interactions with one of the Zn^{2+} ions (bound to P1 in **Ga-GUL** and P1′ in **F-GUL**). Several strong hydrogen bonds and salt bridges are formed with the receptor (Arg198, Arg539, Tyr544, and Gly195 backbone NH) which stabilize the complex and remain intact throughout the MD simulation. These are similar to those observed for **F-GUL**; however, **F-GUL** forms several additional interactions. Arg198 and Tyr544, are particularly important and form key interactions with all three probes (**Figure 9f)**. **Cy3-GUL** again

shows slightly greater fluctuation in the RMSD, largely due to the flexibility in the dye and linker domains due to their less charged nature.

Cy3-GUL shows stronger affinity for mGluR8 than for any of the other mGluRs (**Figure 29e, Table 3-4**), adopting a bound conformation distinct from that of the other two probes (**Figure 29f**) with the **GUL** moiety buried deep within the highly charged cleft (**Figure 29e**). Three extremely stable salt bridges are formed between the P1, P1′ and P1″ carboxylates and the Arg255, and Arg188, and Arg255 of the second subunit (Figure 9**I**). Due to these key interactions, minimal RMSD fluctuations are observed in the RMSD of the MD of the **Cy3-GUL**–mGluR8 complex. With both sufficient predicted binding, and close agreement in the binding mode of the GUL pharmacophore to those of the clinical radiolabels, this probe was synthesized for *in vitro* evaluation, which we accomplished from GUL and our previously prepared cyanine dye (**Figure 30** and accompanying discussion) [51].

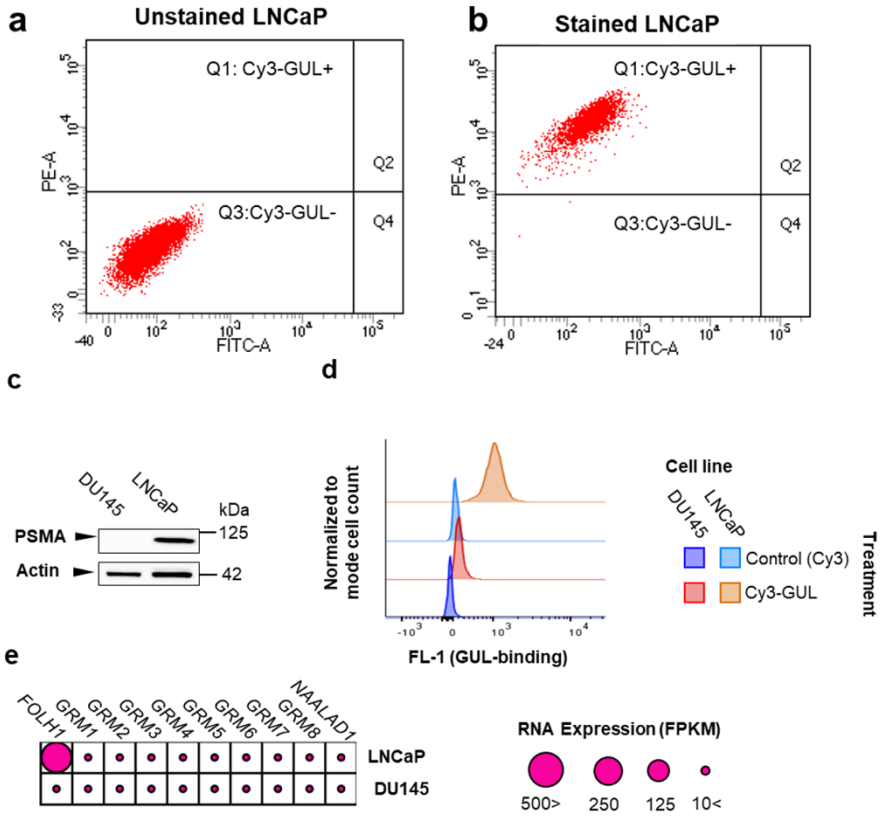

Figure 30 Cy3-GUL binds PSMA The Cy3-GUL probe binds to PSMA-positive cell line (LNCaP) and has no affinity to PSMA-negative cells (DU145).
Cells incubated with 100 nM Cy3-GUL for 1 hour. (a-b) Unstained LNCaP are used to determine the background autofluorescence to set the negative population allowing cells stained with Cy3-GUL to be visualized. (c) Western blot analyses of PSMA levels in LNCaP and DU145 cell lines. (d) The harvested cells were analyzed by flow cytometer. (e) The expression levels of GRMs and NAALADL1 in the studied cell lines.

3.5. Cy3-GUL binds to PSMA *in vitro*.

Flow cytometry demonstrates far stronger uptake of **Cy3-GUL** into PSMA-positive LNCaP cells relative to into PSMA-negative DU145 cells (Figure 30**a-b**). This indicates that although **Cy3-GUL** is predicted to bind well to three different proteins, it is not generally promiscuous: it requires PSMA to enter the cell (both DU145 and LNCaP have low levels of both mGluRs and NAALADL, Figure 30**e)**. In addition, the PSMA-positive LNCaP do not become fluorescent when they are exposed to the unconjugated dye indicating the GUL moiety is essential for selective uptake (Figure 30**d**). Similarly, PSMA-negative DU145 cells, an AdPC cell line, show almost no **Cy3-GUL** uptake (Figure 30**c-d**). Functionally, **Cy3-GUL** exposure shows no cellular toxicity at any tested dose regardless of cell type (Figure 31). This data, along with the computational modeling, suggests that **Cy3-GUL** is an acceptable fluorescent homologue of the two clinically deployed PET reagents; we consequently used it to validate our hypothesis that GUL-probes bind mGluR8 and NAALADL1.

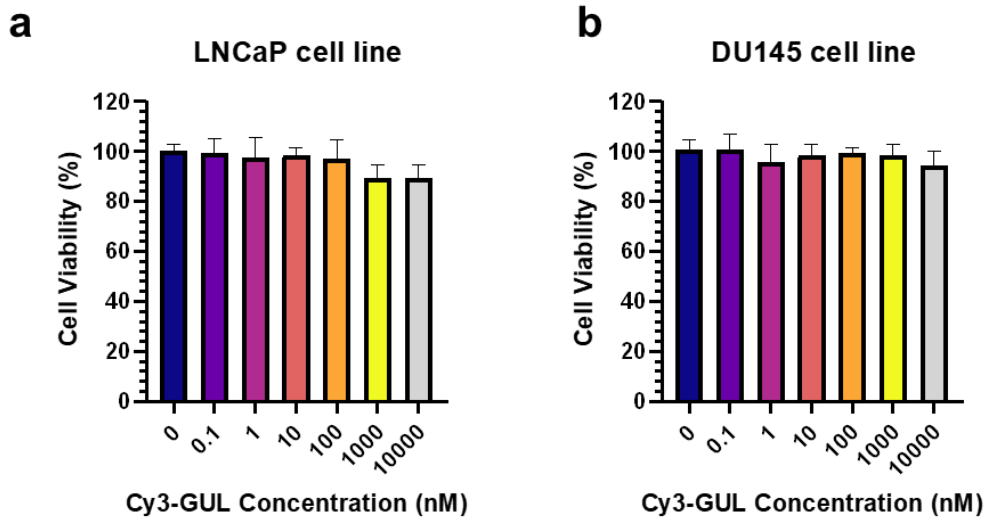

Figure 31 Cy3-GUL is non-cytotoxic at relevant concentrations Cytotoxicity of Cy3-GUL was not observed in (a) LNCaP and (b) DU145 cell lines at concentrations ≤10 μM after 24 h of incubation and washed with PBS.

3.6. Cy3-GUL Probes are selectively taken up by mGLuR and NAALADaseL1.

To investigate the affinity of GUL for mGluR8, we measured the uptake of **Cy3-GUL** in PSMA-negative DU145 cells both with and without overexpression of mGluR8 (Figure 32**a-c**). LNCaP-PSMA positive cells were used as a positive control. Immunofluorescence microscopy demonstrates a five-fold increase in **Cy3-GUL** uptake when mGLuR8 was overexpressed (Figure 32**c**). mGluR8's involvement is further supported by its upregulation when PSMA-negative DU145 cells are driven to develop NE features by epidermal growth factor (EGF) and dibutyryl cAMP (db-cAMP) co-treatment and simultaneous serum starvation as previously described (Figure 32**d &** Figure 33**a-b**).[98] After treatment, cells display neuronal /neuroendocrine characteristics including neurite-like outgrowth (Figure 33**c**), while increasing their expression of select mGluR genes (including *GRM4 and 8*) (Figure 33**c**). Similarly, differential expression of GRMs was observed following overexpression of SRRM4 as a regulator of NEPC (Figure 34). Although not expressing PSMA, these cells still significantly increase their uptake of **Cy3-GUL** (Figure 32**d-f**), supporting our contentions that GUL radiolabels may bind mGluRs such as mGLuR8, and that these mGluRs could be markers of NEPC emergence.

To determine whether NAALADaseL1 can bind **Cy3-GUL**, we performed a knockdown of *NAALADL1* in wild-type LNCaP cells and LNCaP cells driven to a neuroendocrine phenotype (LNCaP-NE) after treatment with charcoal-

stripped serum as previously described[47](Figure 35 and Figure 32**g-i**). PCR analysis both confirmed the successful *NAALADL1* knockdown and demonstrated that *NAALADL1* gene expression is significantly higher in the LNCaP-NE line over control (Figure 32**h**). When treated with the probe, **Cy3-GUL** uptake positively correlated with NAALADaseL1 levels. **Cy3-GUL** uptake was significantly reduced in LNCaP-NE cells with *NAALADL1* knockdown; however, probe uptake was unchanged in wildtype LNCaP cells despite successful knockdown (Figure 32**i**). This is likely due to high PSMA expression in LNCaP control cells which was unaffected by *NAALADL1* knockdown (Figure 32**g,i**).

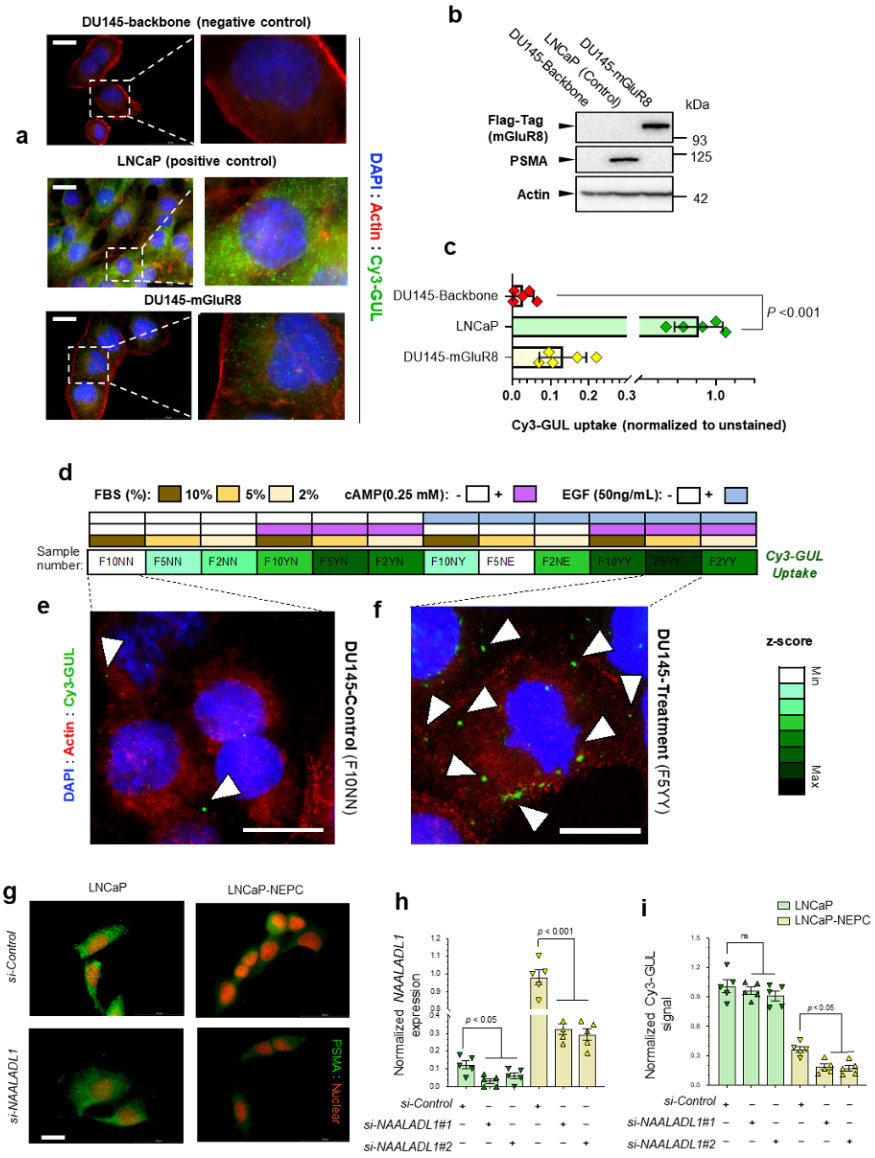

Figure 32 NAALADaseL and MGluR8 regulate update of Cy3-GUL. The overexpression of mGLuR8 in a PSMA-negative cell line induces uptake of Cy3-GUL.

(a) Representative immunocytochemistry images of cells stained with Hoechst (blue), Cy3-GUL (green) and actin (red). (b) Western blot analyses of PSMA and mGluR8 protein levels; (c) Quantification of Cy3-GUL uptake, analyzed by one-way ANOVA; (d) NE-transdifferentiation of DU145 cell line by EGF/cAMP treatment and serum starvation increases Cy3-GUL uptake. DU145 cell line treated with cAMP (0.25 mM), and EGF (50 ng/mL) and gradient levels of FBS while the control group (F10NN model) was treated with 10% FBS. Then after 3 days, the cells were incubated with 100 nM Cy3-

GUL for 1 hour and analyzed by PCR and immunocytochemistry; (e-f) Representative immunocytochemistry images of cells stained with Hoechst (blue), Cy3-GUL (green) and actin (red). The *NAALADL1* gene is upregulated in NEPC cell line model and its inhibition could suppress GUL-ligand uptake; (g) Representative images of Cy3-GUL uptake in AdPC and NEPC models of LNCaP cell lines following inhibition of *NAALADL1* gene using siRNA technology. Scale bar = 20 microns; (h) Quantification of *NAALADL1* gene expression using real time PCR; (i) Quantification of Cy3-GUL uptake following inhibition of *NAALADL1* gene by flow cytometry.

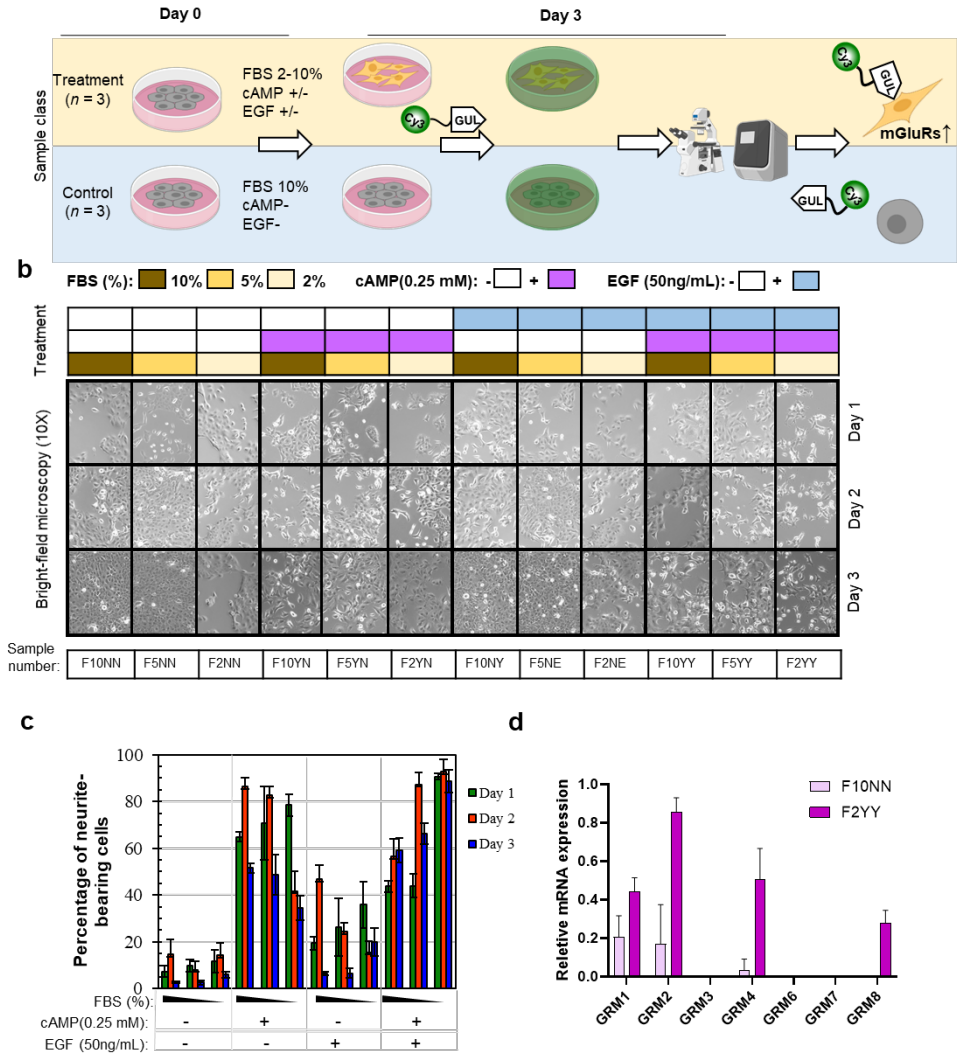

Figure 33 Induction of NE-transdifferentiation is associated with higher Cy3-GUL uptake and a differential expression of mGLuRs.
(a) The treatment group was exposed to a cAMP (0.25 mM), and EGF (50 ng/mL) and gradient levels of FBS while the control group was treated with 10% FBS. After 3 days cells were incubated with 100 nM Cy3-GUL for 1 h and analyzed by PCR and immunocytochemistry. (b) Brightfield microscopy of treated cells demonstrates the morphology and confluency of cells following treatment in each cohort for 3 days. (c) Neurites were studied under an inverted microscope and percentage of cells with neurites counted over 3 fields of view over 3 separate experiments using ImageJ software. (d) Expression of GRMs were measured in F10NN (Control) and F2YY (Treated) models by RT-PCR.

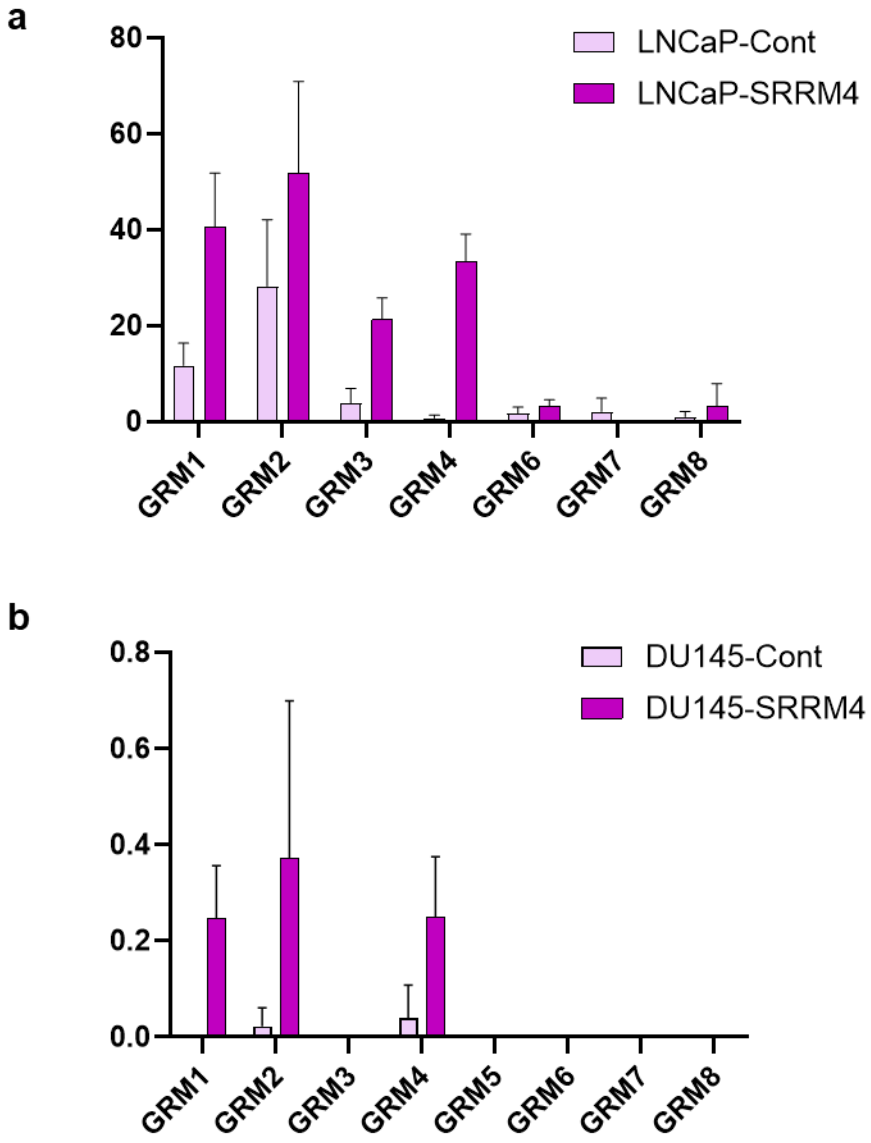

Figure 34 Induction of NE-transdifferentiation by overexpression of SRRM4 is correlated with a differential expression of mGluRs This occurs in both the (a) LNCaP and (b) DU15 cell lines.

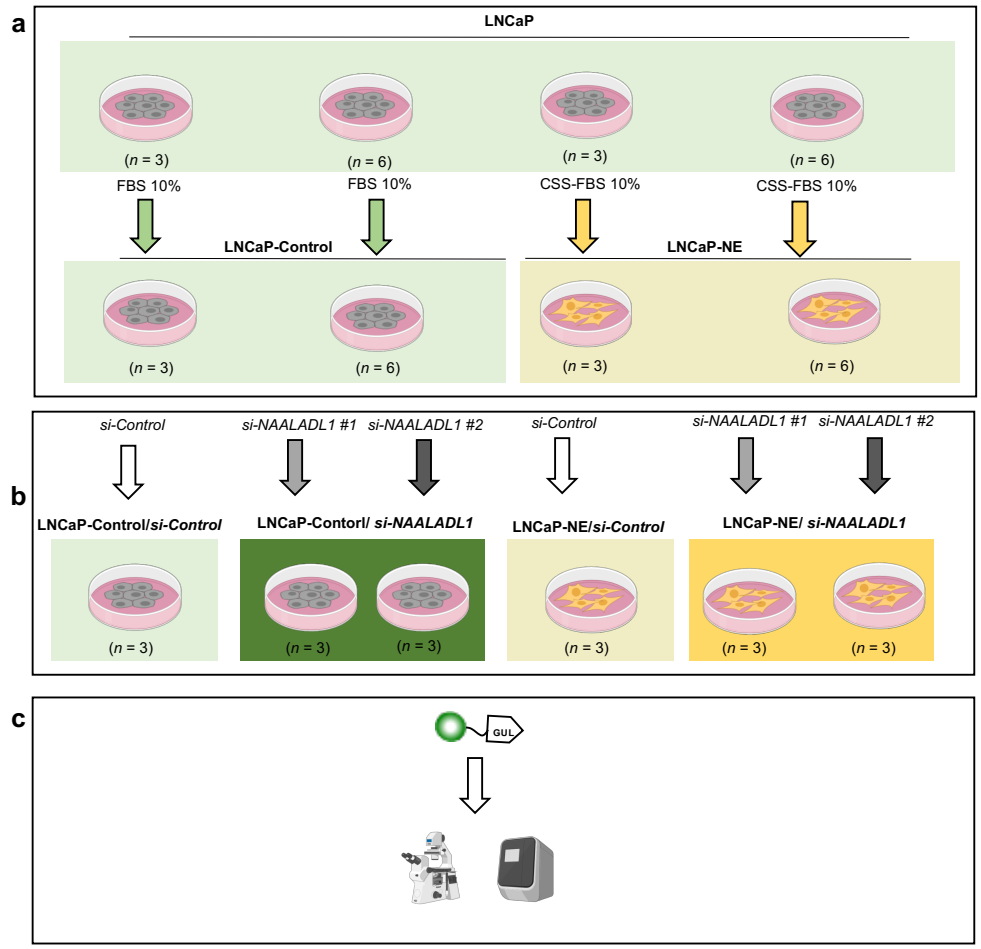

Figure 35 NAALADL1 knockdown in a NE-induced LNCaP cell line.
(a) A schematic representation of the steps required for the progression of the HSPC LNCaP cell line to NEPC. FBS = Fetal bovine serum; CSS = Charcoal-stripped serum. (b) To knockdown human NAALADL1, the small interfering RNA (siRNA)-mediated knockdown was were designed by using two different *si-NAALADL1* named as *si-NAALADL1 #1* and *si-NAALADL1 #2*. Then the scrambled siRNA sequences were used as *si-Control*. The siRNA sequences are listed on Table 1. (c) The resulted four different samples including LNCaP-Control/*si-Control,* LNCaP-Control/ *si-NAALADL1,* LNCaP-NE/*si-Control* and LNCaP-NE/ *si-NAALADL1* incubated with 100 nM Cy3-GUL for 1 h and analyzed by PCR, flow cytometry and immunocytochemistry.

4. Conclusion

Clinical Relevance

National Comprehensive Cancer Network (NCCN) Clinical Practice Guidelines in Oncology (NCCN Guidelines®) currently recommend consideration of platinum-based chemotherapy regimens for NEPC. Therefore, there is no known successful next line therapy for patients NEPC particularly after platinum-based chemotherapy [99]. Especially, AR and PSMA-negativity of NEPC has been a rational for exclusion of PSMA-targeted therapy for NEPC tumors. However, a very recent study demonstrated that GUL-based imaging can delineate IHC validated PSMA-negative metastatic tumors despite the tumour's PSMA-negativity [56]. Comparably, another recent clinical study demonstrated neuroendocrine biomarker levels do not effectively predict outcome of GUL-targeted radioligand therapy [57]. In this work, we showed GUL-targeted PET ligand can be used for imaging of PSMA-negative prostate cancers such as NEPC. Therefore, this work is a rational to include NEPC patients in PSMA-targeted clinical trials. Our result suggests PSMA-targeted therapy could be a possible treatment option for a subset of PSMA-negative patients and NEPC tumors with elevation of PSMA-like proteins such as mGluR8 and NAALADL1.

Limitations and Future Perspective

This work demonstrated that GUL-driven probes bind to NAALADL1 active sites and mGluR8 cleft while not specifically designed for targeting these

proteins. Therefore, the identified interactions between PSMA-like proteins and tracers can be enhanced by using more specific targeting moieties in the structure of probes. In the future studies, we can develop probes to specially target relevant targets such as NAALADL1 and mGluR8 to maximize the efficacy of PSMA-negative tumors.

In fluorescence *in vitro* imaging of this study, we conjugated Cy3 dye with GUL small molecular. This probe is an ideal tool to delineate GUL interactions with PSMA and PSMA-like proteins at cellular level. However, Cy3 is not a recommended option for *in vivo* molecular imaging due to tissue absorbance of Cy3 signal. Thus, for our future animal studies, a feasible approach could be the application of near infrared (NIR) fluorophores in conjugation with GUL. NIR imaging has lower tissue absorbance, scattering, and autofluorescence which facilitates *in vivo* imaging.

Summary

As advanced prostate cancer cells develop low-PSMA profile and/or neuroendocrine features, PSMA-like proteins such as mGLuR and NAALADaseL1 are upregulated while PSMA-levels fall. The computational data suggests that the GUL probes can bind to these proteins, and they may be responsible for GUL probes' recognition of PSMA-negative metastatic NEPC lesions. Fluorescent analogue Cy3-GUL binds to these proteins, validating them as off-target binding targets of GUL.

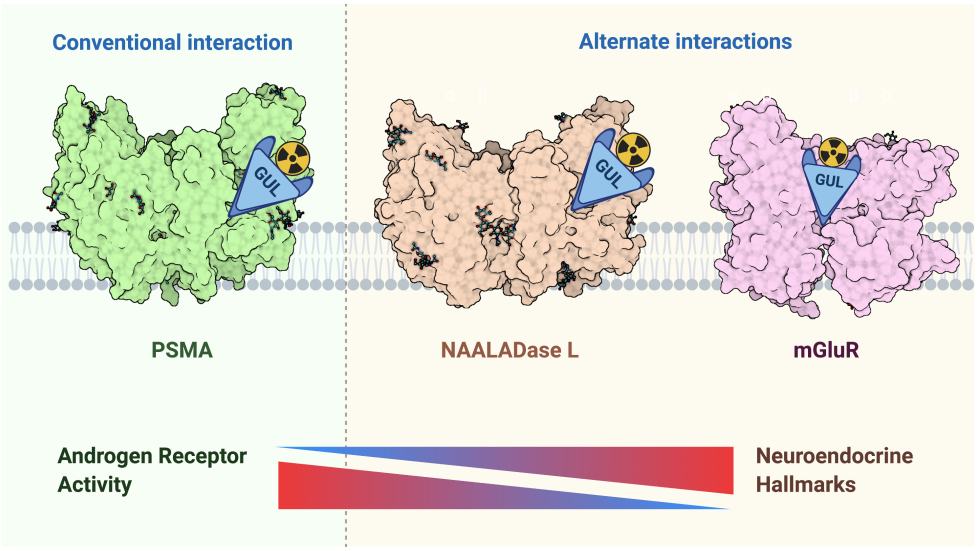

Figure 36 A schematic summary of this Ph.D. Dissertation.
This Ph.D. Dissertation highlights the benefits of integrating computational and synthetic chemistry, with data-mining clinical databases and conducting *in vitro* and *in vivo* experiments to accelerate the validation of protein targets. This work explains why caution must be taken on clinical conclusions made with PSMA-targeted imaging alone and suggests that mGLuR and NAALADaseL1 may represent new targets for imaging and therapeutic purposes. These proteins may play a role in NEPC, and their biochemical importance to this cancer deserves greater attention.

References

1. Siegel, R.L., et al., *Colorectal cancer statistics, 2020.* CA: a cancer journal for clinicians, 2020. **70**(3): p. 145-164.
2. Perner, S., et al., *Adaptive responses of androgen receptor signaling in castration-resistant prostate cancer.* Oncotarget, 2015. **6**(34): p. 35542-55.
3. Chandrasekar, T., et al., *Targeting molecular resistance in castration-resistant prostate cancer.* BMC Med, 2015. **13**: p. 206.
4. Heidenreich, A., et al., *EAU guidelines on prostate cancer. Part II: Treatment of advanced, relapsing, and castration-resistant prostate cancer.* Eur Urol, 2014. **65**(2): p. 467-79.
5. Kiess, A.P., et al., *Prostate-specific membrane antigen as a target for cancer imaging and therapy.* Quarterly Journal of Nuclear Medicine and Molecular Imaging, 2015. **59**(3): p. 241-268.
6. Rai, B.P., et al., *The Role PET with 68 Gallium (Ga)-Labelled Prostate-Specific Membrane Antigen (PSMA) in the Management of Patient with Organ Confined and Locally Advanced Prostate Cancer Prior to Radical Treatment and after Radical Prostatectomy.* Urology, 2016.
7. Ananias, H.J., et al., *Expression of the gastrin-releasing peptide receptor, the prostate stem cell antigen and the prostate-specific membrane antigen in lymph node and bone metastases of prostate cancer.* The Prostate, 2009. **69**(10): p. 1101-1108.
8. Minner, S., et al., *High level PSMA expression is associated with early PSA recurrence in surgically treated prostate cancer.* The Prostate, 2011. **71**(3): p. 281-288.
9. Rybalov, M., et al., *PSMA, EpCAM, VEGF and GRPR as imaging targets in locally recurrent prostate cancer after radiotherapy.* International journal of molecular sciences, 2014. **15**(4): p. 6046-6061.
10. Carlucci, G., et al., *68Ga-PSMA-11 NDA approval: a novel and successful academic partnership.* Journal of Nuclear Medicine, 2021. **62**(2): p. 149-155.
11. Akhtar, N.H., et al., *Prostate-specific membrane antigen-based therapeutics.* Advances in urology, 2011. **2012**.
12. Lutje, S., et al., *PSMA Ligands for Radionuclide Imaging and Therapy of Prostate Cancer: Clinical Status.* Theranostics, 2015. **5**(12): p. 1388-401.

13. Vargas, H., et al., *Molecular imaging of prostate cancer: translating molecular biology approaches into the clinical realm.* European Radiology, 2015. **25**(5): p. 1294-1302.
14. Morigi, J.J., et al., *Prospective comparison of 18F-fluoromethylcholine versus 68Ga-PSMA PET/CT in prostate cancer patients who have rising PSA after curative treatment and Are being considered for targeted therapy.* Journal of Nuclear Medicine, 2015. **56**(8): p. 1185-1190.
15. Giesel, F.L., et al., *PSMA PET/CT with Glu-urea-Lys-(Ahx)-[(6)(8)Ga(HBED-CC)] versus 3D CT volumetric lymph node assessment in recurrent prostate cancer.* Eur J Nucl Med Mol Imaging, 2015. **42**(12): p. 1794-800.
16. Afshar-Oromieh, A., et al., *The diagnostic value of PET/CT imaging with the (68)Ga-labelled PSMA ligand HBED-CC in the diagnosis of recurrent prostate cancer.* Eur J Nucl Med Mol Imaging, 2015. **42**(2): p. 197-209.
17. Ebenhan, T., et al., *Development of a Single Vial Kit Solution for Radiolabeling of 68Ga-DKFZ-PSMA-11 and Its Performance in Prostate Cancer Patients.* Molecules, 2015. **20**(8): p. 14860-78.
18. Sterzing, F., et al., *(68)Ga-PSMA-11 PET/CT: a new technique with high potential for the radiotherapeutic management of prostate cancer patients.* Eur J Nucl Med Mol Imaging, 2016. **43**(1): p. 34-41.
19. Kratochwil, C., et al., *[177Lu] Lutetium-labelled PSMA ligand-induced remission in a patient with metastatic prostate cancer.* European journal of nuclear medicine and molecular imaging, 2015. **42**(6): p. 987-988.
20. Afshar-Oromieh, A., et al., *The Theranostic PSMA Ligand PSMA-617 in the Diagnosis of Prostate Cancer by PET/CT: Biodistribution in Humans, Radiation Dosimetry, and First Evaluation of Tumor Lesions.* Journal of Nuclear Medicine, 2015. **56**(11): p. 1697-1705.
21. Delker, A., et al., *Dosimetry for 177Lu-DKFZ-PSMA-617: a new radiopharmaceutical for the treatment of metastatic prostate cancer.* European journal of nuclear medicine and molecular imaging, 2016. **43**(1): p. 42-51.
22. Szabo, Z., et al., *Initial Evaluation of [(18)F]DCFPyL for Prostate-Specific Membrane Antigen (PSMA)-Targeted PET Imaging of Prostate Cancer.* Mol Imaging Biol, 2015. **17**(4): p. 565-74.
23. Herrmann, K., et al., *Biodistribution and radiation dosimetry for a novel probe targeting prostate specific membrane antigen for Imaging and*

Therapy (68Ga-PSMA I&T). Journal of Nuclear Medicine, 2015: p. jnumed. 115.156133.

24. Kratochwil, C., et al., *PMPA for nephroprotection in PSMA-targeted radionuclide therapy of prostate cancer.* Journal of Nuclear Medicine, 2015. **56**(2): p. 293-298.
25. Weineisen, M., et al., *68Ga-and 177Lu-labeled PSMA I&T: optimization of a PSMA-targeted theranostic concept and first proof-of-concept human studies.* Journal of Nuclear Medicine, 2015. **56**(8): p. 1169-1176.
26. Zippel, C., et al., *Current Status of PSMA-Radiotracers for Prostate Cancer: Data Analysis of Prospective Trials Listed on ClinicalTrials.gov.* Pharmaceuticals, 2020. **13**(1): p. 12.
27. Lesniak, W.G., et al., *Evaluation of PSMA-targeted PAMAM dendrimer nanoparticles in a murine model of prostate cancer.* Mol. Pharm., 2019. **16**(6): p. 2590-2604.
28. Baranski, A.C., et al., *PSMA-11-derived dual-labeled PSMA inhibitors for preoperative PET iaging and precise fluorescence-guided surgery of prostate cancer.* J. Nucl. Med., 2018. **59**(4): p. 639-645.
29. Eder, M., et al., *68Ga-Complex lipophilicity and the targeting property of a Urea-based PSMA inhibitor for PET imaging.* Bioconjugate Chem., 2012. **23**(4): p. 688-697.
30. Ganguly, T., et al., *A high-affinity [(18)F]-labeled phosphoramidate peptidomimetic PSMA-targeted inhibitor for PET imaging of prostate cancer.* Nucl. Med. Biol., 2015. **42**(10): p. 780-787.
31. Kuten, J., et al., *Head- to head comparison of ^{68}Ga-PSMA-11 with ^{18}F-PSMA-1007 PET/CT in staging prostate cancer using histopathology and immunohistochemical analysis as reference-standard.* J. Nucl. Med., 2019.
32. Cardinale, J., et al., *Procedures for the GMP-compliant production and quality control of [^{18}F]PSMA-1007: A next generation radiofluorinated tracer for the detection of prostate cancer.* Pharmaceuticals (Basel, Switzerland), 2017. **10**(4): p. 77.
33. O'Keefe, D.S., et al., *Mapping, genomic organization and promoter analysis of the human prostate-specific membrane antigen gene.* Biochim Biophys Acta, 1998. **1443**(1-2): p. 113-27.
34. Chang, S.S., *Overview of Prostate-Specific Membrane Antigen.* Reviews in Urology, 2004. **6**(Suppl 10): p. S13-S18.
35. Israeli, R.S., et al., *Expression of the prostate-specific membrane antigen.*

Cancer research, 1994. **54**(7): p. 1807-1811.

36. Wright, G.L., et al., *Upregulation of prostate-specific membrane antigen after androgen-deprivation therapy.* Urology, 1996. **48**(2): p. 326-334.
37. Good, D., et al., *Cloning and characterization of the prostate-specific membrane antigen promoter.* Journal of cellular biochemistry, 1999. **74**(3): p. 395-405.
38. Watt, F., et al., *A tissue-specific enhancer of the prostate-specific membrane antigen gene, FOLH1.* Genomics, 2001. **73**(3): p. 243-254.
39. Noss, K.R., S.A. Wolfe, and S.R. Grimes, *Upregulation of prostate specific membrane antigen/folate hydrolase transcription by an enhancer.* Gene, 2002. **285**(1-2): p. 247-56.
40. Yu, J., et al., *An Integrated Network of Androgen Receptor, Polycomb, and TMPRSS2-ERG Gene Fusions in Prostate Cancer Progression.* Cancer cell, 2010. **17**(5): p. 443-454.
41. Evans, M.J., et al., *Noninvasive measurement of androgen receptor signaling with a positron-emitting radiopharmaceutical that targets prostate-specific membrane antigen.* Proceedings of the National Academy of Sciences, 2011. **108**(23): p. 9578-9582.
42. DiPippo, V.A., et al., *In vivo efficacy of PSMA ADC in combination with enzalutamide in castration-resistant prostate cancer.* Cancer Research, 2015. **75**(15 Supplement): p. 1685-1685.
43. Bakht, M.K., et al., *Influence of Androgen Deprivation Therapy on the Uptake of PSMA-Targeted Agents: Emerging Opportunities and Challenges.* Nucl Med Mol Imaging, 2017. **51**(3): p. 202-211.
44. Kaittanis, C., et al., *Prostate-specific membrane antigen cleavage of vitamin B9 stimulates oncogenic signaling through metabotropic glutamate receptors.* J. Exp. Med., 2017. **215**(1): p. 159-175.
45. Bakht, M.K., et al., *Influence of androgen deprivation therapy on the uptake of PSMA-targeted agents: Emerging opportunities and challenges.* Nuc. Med. Molec. Imag., 2017. **51**(3): p. 202-211.
46. Hupe, M.C., et al., *Expression of prostate-specific membrane antigen (PSMA) on biopsies is an independent risk stratifier of prostate cancer patients at time of initial diagnosis.* Front. Oncol., 2018. **8**: p. 623.
47. Bakht, M.K., et al., *Neuroendocrine differentiation of prostate cancer leads to PSMA suppression.* Endocr. Relat. Cancer, 2019. **26**(2): p. 131-146.
48. Beltran, H., et al., *Divergent clonal evolution of castration-resistant*

neuroendocrine prostate cancer. Nat. Med., 2016. **22**(3): p. 298-305.

49. Bakht, M.K., et al., *Neuroendocrine differentiation of prostate cancer leads to PSMA suppression.* Endocrine-related cancer, 2019. **26**(2): p. 131-146.
50. Bluemn, E.G., et al., *Androgen receptor pathway-independent prostate cancer is sustained through FGF signaling.* Cancer Cell, 2017. **32**(4): p. 474–489.
51. Bakht, M.K., et al., *Differential expression of glucose transporters and hexokinases in prostate cancer with a neuroendocrine gene signature: a mechanistic perspective for FDG imaging of PSMA-suppressed tumors.* J. Nuc. Med., 2020. **61**(6): p. 904-910.
52. Paschalis, A., et al., *Prostate-specific membrane antigen heterogeneity and DNA repair defects in prostate cancer.* Eur. Urol., 2019. **76**(4): p. 469-478.
53. Spratt, D.E., et al., *Utility of FDG-PET in clinical neuroendocrine prostate cancer.* Prostate, 2014. **74**(11): p. 1153–1159.
54. Thang, S.P., et al., *Poor outcomes for patients with metastatic castration-resistant prostate cancer with low prostate-specific membrane antigen (PSMA) expression deemed ineligible for 177Lu-labelled PSMA radioligand therapy.* Eur. Urol. Oncol., 2018. **in press**.
55. Bakht, M.K., et al., *Differential expression of glucose transporters and hexokinases in prostate cancer with a neuroendocrine gene signature: a mechanistic perspective for FDG imaging of PSMA-suppressed tumors.* Journal of Nuclear Medicine, 2019: p. jnumed. 119.231068.
56. Iravani, A., et al., *Molecular imaging of neuroendocrine differentiation of prostate cancer: a case series.* Clinical Genitourinary Cancer, 2021.
57. Derlin, T., et al., *Neuroendocrine differentiation and response to PSMA-targeted radioligand therapy in advanced metastatic castration-resistant prostate cancer: A single-center retrospective study.* J. Nucl. Med., 2020.
58. Current, K., et al., *Investigating PSMA-targeted radioligand therapy efficacy as a function of cellular PSMA levels and intra-tumoral PSMA heterogeneity.* Clin. Cancer Res., 2020.
59. Fendler, W.P., et al., *False positive PSMA PET for tumor remnants in the irradiated prostate and other interpretation pitfalls in a prospective multi-center trial.* Eur. J. Nucl. Med. Mol. Imaging, 2020.
60. Walter, A., et al., *Correlated Multimodal Imaging in Life Sciences: Expanding the Biomedical Horizon.* Frontiers in Physics, 2020. **8**(47).
61. Kroeze, W.K., et al., *PRESTO-Tango as an open-source resource for*

interrogation of the druggable human GPCRome. Nat. Struct. Mol. Biol., 2015. **22**(5): p. 362-9.

62. Ichihara, M., et al., *Thermodynamic instability of siRNA duplex is a prerequisite for dependable prediction of siRNA activities.* Nucleic Acids Res., 2007. **35**(18): p. e123.
63. Camacho, C., et al., *BLAST+: architecture and applications.* BMC Bioinformatics, 2009. **10**: p. 421.
64. Guzenko, D., S.K. Burley, and J.M. Duarte, *Real time structural search of the Protein Data Bank.* PLOS Computational Biology, 2020. **16**(7): p. e1007970.
65. Beltran, H., et al., *Whole-Exome Sequencing of Metastatic Cancer and Biomarkers of Treatment Response.* JAMA Oncol., 2015. **1**(4): p. 466-74.
66. Sailer, V., et al., *Integrative molecular analysis of patients with advanced and metastatic cancer.* JCO Precis. Oncol., 2019. **3**.
67. Beltran, H., et al., *Divergent clonal evolution of castration resistant neuroendocrine prostate cancer.* Nat. Med., 2016. **22**(3): p. 298-305.
68. Robinson, D., et al., *Integrative clinical genomics of advanced prostate cancer.* Cell, 2015. **161**(5): p. 1215-1228.
69. Dunning, M.J., et al., *Mining human prostate cancer datasets: The "camcAPP" Shiny App.* EBioMedicine, 2017. **17**: p. 5-6.
70. Hothorn, T., K. Hornik, and A. Zeileis, *Unbiased recursive partitioning: A conditional inference framework.* J. Comput. Graph. Stat., 2006. **15**(3): p. 651-674.
71. Akamatsu, S., et al., *The placental gene PEG10 promotes progression of neuroendocrine prostate cancer.* Cell Rep., 2015. **12**(6): p. 922-936.
72. Ci, X., et al., *Heterochromatin protein 1a mediates development and aggressiveness of neuroendocrine prostate cancer.* Cancer Res., 2018. **78**(10): p. 2691-2704.
73. Li, Y., et al., *SRRM4 drives neuroendocrine transdifferentiation of prostate adenocarcinoma under androgen receptor pathway inhibition.* Eur. Urol., 2017. **71**(1): p. 68-78.
74. Nabavi, N., et al., *miR-100-5p Inhibition induces apoptosis in dormant prostate cancer cells and prevents the emergence of castration-resistant prostate cancer.* Sci. Rep., 2017. **7**: p. 4079.
75. Lin, D., et al., *High fidelity patient-derived xenografts for accelerating prostate cancer discovery and drug development.* Cancer Res., 2014. **74**(4):

p. 1272-1283.

76. Maresca, K.P., et al., *A series of halogenated heterodimeric inhibitors of prostate specific membrane antigen (PSMA) as radiolabeled probes for targeting prostate cancer.* J. Med. Chem., 2009. **52**(2): p. 347-357.

77. Sippl, M.J. and M. Wiederstein, *Detection of spatial correlations in protein structures and molecular complexes.* Structure, 2012. **20**(4): p. 718-728.

78. Friesner, R.A., et al., *Glide: A new approach for rapid, accurate docking and scoring. 1. Method and assessment of docking accuracy.* J. Med. Chem., 2004. **47**(7): p. 1739-1749.

79. *QikProp 2019-03*. 2019, Schrödinger: New York, NY.

80. Reddy, K.K., P. Singh, and S.K. Singh, *Blocking the interaction between HIV-1 integrase and human LEDGF/p75: mutational studies, virtual screening and molecular dynamics simulations.* Mol. BioSyst., 2014. **10**(3): p. 526-536.

81. *LigPrep 2019-03*. 2019, Schrödinger: New York, NY,.

82. *Induced Fit Docking protocol; Glide and Prime*. 2019, Schrödinger,: New York, NY.

83. *Prime, version 2000-3.* 2020, Schrödinger: New York.

84. Jakalian, A., D.B. Jack, and C.I. Bayly, *Fast, efficient generation of high-quality atomic charges. AM1-BCC model: II. Parameterization and validation.* J. Comput. Chem., 2002. **23**(16): p. 1623-1641.

85. Li, P. and K.M. Merz, *MCPB.py: A python based metal center parameter builder.* J. Chem. Inform. Model., 2016. **56**(4): p. 599-604.

86. Ding, Y., et al., *Inhibition of nischarin expression promotes neurite outgrowth through regulation of PAK activity.* PLOS ONE, 2015. **10**(12): p. e0144948.

87. Youn, S., et al., *Carborane-containing urea-based inhibitors of glutamate carboxypeptidase II: Synthesis and structural characterization.* Bioorg. Med. Chem. Lett., 2015. **25**(22): p. 5232-5236.

88. Pavlicek, J., J. Ptacek, and C. Barinka, *Glutamate carboxypeptidase II: An overview of structural studies and their importance for structure-based drug design and deciphering the reaction mechanism of the enzyme.* Curr. Med. Chem., 2012. **19**(9): p. 1300-9.

89. Machulkin, A.E., et al., *Small-molecule PSMA ligands. Current state, SAR and perspectives.* J. Drug Target., 2016. **24**(8): p. 679-93.

90. Barinka, C., et al., *Interactions between human glutamate carboxypeptidase*

II and urea-based inhibitors: Structural characterization. J. Med. Chem., 2008. **51**(24): p. 7737-7743.

91. Mesters, J.R., et al., *Structure of glutamate carboxypeptidase II, a drug target in neuronal damage and prostate cancer.* EMBO J., 2006. **25**(6): p. 1375-84.

92. Wu, L.Y., et al., *The molecular pruning of a phosphoramidate peptidomimetic inhibitor of prostate-specific membrane antigen.* Bioorg. Med. Chem., 2007. **15**(23): p. 7434-7443.

93. Novakova, Z., et al., *Unprecedented binding mode of hydroxamate-based inhibitors of glutamate carboxypeptidase II: Structural characterization and biological activity.* J. Med. Chem., 2016. **59**(10): p. 4539-4550.

94. Cardinale, J., et al., *Development of PSMA-1007 - related series of 18F-labeled Glu-ureido type PSMA inhibitors.* J. Med. Chem., 2020: p. ASAP article.

95. Pangalos, M.N., et al., *Isolation and expression of novel human glutamate carboxypeptidases with N-Acetylated α-linked acidic dipeptidase and dipeptidyl peptidase IV activity.* J. Biol. Chem., 1999. **274**(13): p. 8470-8483.

96. Abida, W., et al., *Genomic correlates of clinical outcome in advanced prostate cancer.* Proc. Natl. Acad. Sci. U. S. A., 2019. **116**(23): p. 11428-11436.

97. Taylor, B.S., et al., *Integrative genomic profiling of human prostate cancer.* Cancer Cell, 2010. **18**(1): p. 11-22.

98. Humez, S., et al., *Epidermal growth factor-induced neuroendocrine differentiation and apoptotic resistance of androgen-independent human prostate cancer cells.* Endocr. Relat. Cancer, 2006. **13**(1): p. 181-195.

99. Yamada, Y. and H. Beltran, *Clinical and Biological Features of Neuroendocrine Prostate Cancer.* Curr Oncol Rep, 2021. **23**(2): p. 15.

Acknowledgements

I declare no competing financial interest. Parts of this work was supported by and a grant from the Korea Health Technology R&D Project through the Korea Health Industry Development Institute (KHIDI), funded by the Ministry of Health and Welfare, Republic of Korea (H18C1916 [Prof. Gi Jeong Cheon]).

Parts of this study was supported by Canadian Institutes of Health Research #142189 (Prof. Lisa Porter) #PJT156150 (Prof. Xuesen Dong), the Natural Sciences and Engineering Research Council of Canada #2018-06338 (Prof. John Trant), the Government of Ontario #ER18-14-114 (Prof. John Trant), the Windsor Cancer Centre Foundation (2017-003 Prof. John Trant), and the Canadian Tricouncil New Frontiers Exploration Fund (Prof. John Trant NFRFE-2018-00075). The financial support of TELUS Ride for Dad, Prostate Cancer Fight Foundation (Prof. Lisa Porter) Banting Research Foundation (Prof. John Trant) is greatly appreciated. Dr. Farsheed Shahbazi-Raz, Mr. Daniel Meister, and Prof. John Trant would like to thank Compute Canada for providing the facilities of the Shared Hierarchical Academic Research Computing Network (SHARCNET: www.sharcnet.ca) to support this project. I would like to appreciate the following scholars for their conurbation to this work:

Conceptualization: *Prof. John Trant, Prof. Lisa Porter, Prof. Gi Jeong Cheon and Prof. Keon Wook Kang;* Funding acquisition: *Prof. John Trant, Prof. Lisa Porter, Prof. Gi Jeong Cheon and Prof. Keon Wook Kang, Prof. Yuzhuo*

Wang, Prof. Xuesen Dong; Investigation: *Dr. John Hayward, Dr. Farsheed Shahbazi-Raz, Mr. Daniel Meister, Mr. Adam Pillon, Mr. Mathew Stover, Mr. Adam Tronchin, Ms. Lavleen Mader, Dr. Bre-Anne Fifield and Dr. Sheng-Yu Ku;* Methodology: *Farsheed Shahbazi-Raz, Mr. Daniel Meister*; Project administration: *Prof. John Trant, Prof. Lisa Porter, Prof. Gi Jeong Cheon and Prof. Keon Wook Kang*; Supervision: *Prof. John Trant, Prof. Lisa Porter, Prof. Gi Jeong Cheon and Prof. Keon Wook Kang*; Visualization: *Farsheed Shahbazi-Raz, Mr. Daniel Meister*; Writing: *Dr. John Hayward, Farsheed Shahbazi-Raz, Mr. Daniel Meister*.

국문 초록

막횡단 단백질인 전립선특이막항원 (prostate-specific membrane antigen, PSMA)은 전립선암의 영상 및 치료를 위한 유망한 표적이다. PSMA 는 대부분의 전립선암에서 과발현되며 PSMA 표적 양전자방출단층촬영 (positron emission tomography, PET) 프로브를 사용하여 임상적으로 영상화 할 수 있다. 현재 글루타메이트-우레이도-리신(Glutamate-Ureido-Lysine, GUL) 유도체 방사성 리간드는 PSMA 표적 PET 영상을 위한 선도적인 프로브이다.

신경내분비 전립선암 (neuroendocrine prostate cancer, NEPC)과 같이 높은 사망률, 치료 내성을 보이는 특정 전립선암 부분집단에서는 PSMA 발현이 낮은 편이다. 하지만 GUL 기반 PSMA 표적 프로브는 NEPC 전이성 종양 병변을 잘 검출하는 경우가 보고되고 있다. 이러한 PSMA 발현이 낮은 종양에서 GUL 기반 프로브는 PSMA 가 아닌 비표적 단백질에 결합할 것으로 예상된다. 본 연구에서는, NEPC 를 포함한 진행성 전립선암에서 PSMA 유사 아미노펩티다제 NAALADaseL 및 대사성 글루타메이트 수용체 (mGluR)의 높은 발현을 확인하였다. 또한, mGluRs 의 발현 수준이 PSMA 발현과 역상관 관계가 있으며 불량한 임상 예후와 관련이 있음을 확인하였다. 컴퓨터 계산적 방법을 통해 GUL 기반 프로브의 NAALADaseL 및 mGluRs 에 결합 능력을 예측하였고 in-vitro 형광 프로브를 활용하여 GUL 기반 프로브의 PSMA, NAALADaseL 및 특정 mGluRs 에 대한 우수한 친화성을 검증하였다. 종합하여 볼 때 mGLuR 및 NAALADaseL 은 GUL 기반 프로브의 표적이 될 수 있으며 특히, PSMA 발현이 낮은 NEPC 와 같은 치료저항성 암에 대한 새로운 진단 및 치료 표적이 될 수 있다.

주요어 : 전립선암, 전립선특이막항원, 글루타메이트-우레이도-리신, 양전자방출단층촬영, 대사성 글루타메이트 수용체

학 번 : 2014-31464